AN INTEGRATED YIELD-LINE APPROACH TO TENSILE AND COMPRESSIVE MEMBRANE ACTIONS IN THIN LIGHTLY-REINFORCED CONCRETE SLABS

Ian Burgess[1]* and Billy Chan[2]

[1*] Corresponding Author: Department of Civil and Structural Engineering, University of Sheffield, Sheffield S1 3JD, United Kingdom. (**email: ian.burgess@sheffield.ac.uk*, *Tel. 0044 114 2225060*)

[2] Arup Ltd, Hong Kong.

ABSTRACT

In this paper a recently developed method of analysis is used to examine the effects of rotational and normal continuity at parallel edges on the large-deflection behaviour of lightly reinforced rectangular concrete slabs. The method makes the conventional assumption of an optimal yield-line mechanism at infinitesimal deflection, and subsequently ensures equilibrium of the flat facets of the mechanism using the correct kinematics as the deflection increases. For slabs which are only supported transversely at their edges the method was developed to model the development of tensile membrane action, which enhances the slab's load capacity as its deflection increases, This has particular practical applications in the resistance of buildings to hazard loads, particularly fire. The fracture ductility of reinforcing mesh crossing yield lines is used to monitor the progressive fracture of the mesh across the yield-line cracks. This progressive fracture causes the enhancement of load capacity to have natural limits, depending largely on the bond characteristics of the bars at a discrete crack-face.

When rotational continuity at parallel edges is modelled as an extension to the technique, by forcing plastic hinges to develop along these edges as part of the yield-line mechanism, this enhances the yield-line failure load of the slab, but has no effect on either the geometry of the yield line or the additional load capacity at any value of deflection. However, if these edges are assumed also to be fully restrained so that there can be no outward movement of the slab, the initial yield-line mechanism is immediately subject to compressive membrane action. This can generate a very high initial load capacity, which rapidly declines as the deflection increases, but may subsequently rise slowly as tensile membrane action develops. However, it is essential in all cases that reinforcement has high ductility across yield lines if any significantly rising load capacity is to be generated as the deflection rises.

***Key Words**: tensile membrane action, compressive membrane action, concrete, slabs, yield line theory.*

1. Introduction

The fact that membrane stresses, in combination with flexural through-thickness stress distributions, can enhance the load-carrying capacity of slabs, has been recognized in construction techniques for some time. Perhaps the best example has been the use of internal arching, utilising the curvature of the lines of resultant compression within the thickness of both beams and slabs, in masonry construction. As with other arching mechanisms, this requires boundary restraint to in-plane movement, which generates the necessary horizontal equilibrating reaction forces.

In the early 20th Century the phenomenon of "reverse dome action", usually now referred to as tensile membrane action (TMA) was briefly described by Westergaard and Slater [1] in explaining discrepancies in strength between theory and tests of thin concrete slabs. The fact that lightly-reinforced concrete slabs with two-way support fail at load levels considerably above the predictions given by conventional theories, including yield-line theory, was first identified by Ockleston [2], when reporting on his full-scale tests conducted during the demolition of the Dental Hospital in Johannesburg. In subsequent research [3] he concluded that the observed enhancement was caused by internal arching, or compressive membrane action (CMA) within individual panels restrained in-plane by adjacent panels, rather than by tensile membrane action. In the following decade, major research studies were carried out by Park [4, 5] and by Wood [6], which included both experimental and analytical work. These concerned mainly CMA, and their analytical approaches were based on a strip analogy. During the same period Christiansen [7] published an analytical approach, mainly concerning restrained reinforced concrete beams. Christiansen described CMA for two-way supported slabs, based on an enhancement of deflection after initial failure in terms of Johansen's [8] yield-line theory, but did not then propose an analytical approach. Park recognized the effect of the restraint stiffness of the panel boundary, and carried out a series of tests on slab panels of various dimensions and reinforcement arrangements, including continuity outside the panel supports. He also developed an analytical approach based on the strip analogy to estimate the enhancement of capacity of the slab, which was later extended and refined by Park and Gamble [9]. This method has been the basis for approaches applied to different applications; for instance, utilizing unreserved load capacity in bridge decks (Kirkpatrick et. al. [10]) and enhancing punching shear strength in slabs (Kuang and Morley [11]).

Tensile membrane action is not a complete reversal of compressive membrane action. Whereas CMA depends on horizontal restraint to in-plane movement on opposing edges, TMA is generated by large deflections of simply supported slabs, because the central tension field can be equilibrated by a circumferential compression field without any assistance from edge restraint. Hence, most of the research on TMA has been done on simply supported rectangular concrete slab panels. Both experimental and analytical studies were carried out during the 1960s.

Several researchers developed their own analytical methods to derive the load capacity of slabs under TMA, each of which had its own focus and limitations. Wood [6], Sawczuk and Winnicki [12], Kemp [13] and Hayes [14] and Taylor [15] each proposed approaches to enhancement of strength by TMA due to finite deflections after initial yield-line failure. However, interest in TMA declined after the 1960s, perhaps logically since it was seen as irrelevant to normal design strength calculations for building structures. Interest revived when it became apparent that the mechanism could provide an ultimate safeguard against disproportionate collapse in hazard-loading situations, such as blast and fire. In particular, the series of fire tests on a loaded full-scale 8-storey composite building at Cardington (Kirby [16]; Newman *et al.* [17]) in 1995-96 demonstrated clearly that TMA could provide considerable extra load capacity to floor slabs beyond the stage at which very high temperatures had degraded the strength of the attached downstand steel beams almost completely. The survival of the floors in seven different structural and fire scenarios, where conventional strength calculations, such as Johansen's [8] yield-line theory, indicated failure, conveyed a powerful message to the structural fire engineering community. New design methods, both based on the work of Hayes [14], were put forward by Bailey and Moore [18, 19] and by Clifton and Beck [20]; these have been widely used in performance-based structural fire engineering design. The method of Bailey and Moore has now formed the basis of recommendations by Vassart and Zhao [21, 22]. All of these models use an initial small-deflection yield-line failure mechanism of the non-composite slab, and its associated load capacity, as the starting point for their progressive enhancement of load capacity as the slab deflection increases. Experimental model-scale tests of plain reinforced concrete slabs with both isotropic and orthotropic reinforcement were carried out by Foster *et al.*[23] and by Bailey and Toh [24], at both ambient and elevated temperatures. At about the same time a set of 6 elevated-temperature tests on 3.15m x 4.15m concrete slabs using different decking systems was conducted in New Zealand by Lim and Wade [25], and these were subsequently modelled using the SAFIR software by Lim *et al.* [26]

The first author of this paper developed a new approach [27] to tensile membrane action of concrete slabs, which also begins with the optimal yield-line mechanism. The method counters the objection to all the methods developed from Hayes, that all specify a membrane force distribution across the yield lines which is simply assumed, and does not change with deflection of the slab facets. In addition, the possibility that reinforcing mesh can fracture across opening cracks at the yield lines is not included, although a rather crude averaged measure of rebar strain over the whole length is included in the fire engineering methods. The new approach considers the horizontal equilibrium of the four facets, linking this directly to the kinematics of the displacements and the contact zones between yield lines as displacements increase. This enables the crack-width at any bar position on a discrete yield line to be known, and therefore, if the crack-width at which a bar fractures is known, the effects of progressive failure of mesh are predicted. It is worth noting that all of the approaches require discrete yield lines, rather than yielding which is "smeared" over wide zones. This makes them most appropriate for lightly reinforced slabs such as those

used in combination with downstand steel beams as composite floor panels; at high temperatures the strength of the downstand beams may have degraded (as in some of the Cardington tests) to the extent that these slabs are essentially acting alone. In fact, the first development beyond a basic theory for the new method was to extend its principles directly to composite slab panels in fire conditions [28]. As in most structural fire engineering scenarios, this extension requires a constant applied load intensity and progressively increasing steel beam temperatures. Thus, the enhancement due to TMA is most properly expressed for such cases in terms of the maximum steel beam temperature that can be sustained at any given deflection of the panel for a particular load intensity.

As a further extension of the basic approach for lightly reinforced concrete slab panels, this paper now looks at the effect of continuity with adjacent panels on the large-deflection behaviour under load. Boundary conditions are significant in dictating the load capacity of a slab in terms of its initial yield-line capacity, and have a continued influence at finite deflections. In real structural applications the continuity assumptions of a representative panel represents various situations of panels within a uniformly loaded floor, such as those illustrated in Figure 1.

In terms of an analysis on an individual panel (the lighter panels in the cases of Figure 1) in a design situation the relevant continuity conditions depend very much on the position of the panel within the whole floor layout, and to some extent on the degree of conservatism required. For a corner panel a conservative design approach would be to consider it as a completely isolated panel (Figure 1(a)). For panels containing one perimeter edge the corresponding approach considering a symmetric yield-line mechanism would be to assume continuity across the edges perpendicular to the perimeter (Figures 1(b & c)). An internal panel could be given continuity across all edges (Figure 1(d)). Continuity may of course either be purely rotational, in which case only bending occurs across all yield lines, or it may include axial restraint provided by a large continuous area of surrounding concrete slab. At this stage only bi-symmetric continuity conditions are considered on edges parallel to either the x- or y-axes of the panel, so that only bi-symmetric yield-line patterns are generated. In extensions of the work cases with monosymmetry can be considered.

It is worth mentioning that slab continuity is expressly excluded from the methods developed from Hayes's treatment, on the assumption that mesh is extremely likely to fracture across the hogging yield lines bridging across the undeformed edge supports of composite slabs with thermally weakened internal steel beams. This was done as an explicitly conservative assumption within the method [18, 19] of Bailey and Moore, intended to be used for performance-based structural fire engineering design.

2. Methodology

This paper presents an analytical approach to the large-deflection behaviour and load capacity of transversely loaded, lightly reinforced rectangular concrete slab panels with rotational or in-plane continuity across their boundaries. It is based on the fundamental approach developed by Burgess [27]. It is important to restate the basic assumptions of this analysis, since it is utilized throughout the new approach to continuity of both types across boundaries:

- After a yield-line pattern of discrete plastic hinges has initially developed at small deflection, this pattern does not change as its deflection increases.
- Horizontal equilibrium of all of the flat facets of the slab needs to be maintained by the combination of forces across the yield lines within the slab and across the slab edges.
- These forces are created:
  - as tensile forces from unfractured reinforcing mesh crossing the yield lines at any section where there is a crack separation at the level of the mesh, and the mesh is assumed to act at its yield stress;
  - as compressive forces from the concrete stress blocks on any yield line, where the concrete acts at its compressive strength.
- The zones of concrete contact along any yield line are defined by the kinematics of the slab facets, which rotate compatibly about the slab edges together with some rigid-body movements.
- Reinforcing mesh can fracture across any position on a crack that has a separation greater than the fracture crack-width determined from the ductility of the mesh, its bond characteristics and the spacing between weld-points to transverse bars.

The application of these principles to slabs with only rotational edge-restraint, and to those with both rotational and in-plane edge-restraint, are both considered. However, the basic horizontal equilibrium equations are identical for all cases.

As in the previous papers it is necessary to recognize that the optimum yield-line mechanism of a given slab may have its central yield line aligned in either of the x- or y-directions, depending on the slab's aspect ratio or the orthotropy of its reinforcing mesh; these will be referred to as either "x-aligned" or "y-aligned" mechanisms. For a slab that has isotropic mesh, this yield line is aligned parallel to the longer sides. Obviously, once the alignment of yield lines has been determined, the subsequent equilibrium states could be analysed in a unified fashion by realigning the positional coordinate system so that "x" is always parallel to the central yield line. However, in order to keep the analysis consistent with the previous paper [28], in which attached steel beams always span in the x-direction, the two alignments are treated as distinct, although derivations will not be duplicated. In either case the yield lines are assumed to be discrete, rather than "smeared" with a finite width, and they divide the slab into four separate facets.

2.1 Horizontal equilibrium

The first step is to establish horizontal equilibrium of all these facets under the forces acting on them. All of these in-plane forces are shown in Figure 2 for *x*-aligned conditions, and in Figure 3 for *y*-aligned conditions.

Considering the *x*-aligned case shown in Figure 2, force equilibrium in the *y*-direction for the trapezoidal facets gives:

$$T_{y1} + T_{y2} - T_{y3} = C_1 \sin\gamma - S\cos\gamma + C_{y2} - C_{y3} \tag{1}$$

Similarly, force equilibrium in the *x*-direction for the triangular facets gives:

$$T_{x1} - T_{x4} = C_1 \cos\gamma + S\sin\gamma - C_{x4} \tag{2}$$

Combining (3) and (4) to eliminate S gives:

$$(T_{x1} - T_{x4})\cos\gamma + (T_{y1} + T_{y2} - T_{y3})\sin\gamma = C_1 + (C_{y2} - C_{y3})\sin\gamma - C_{x4}\cos\gamma \tag{3}$$

These equilibrium equations reflect those for an isolated panel [27], but now include the tensile and compressive edge forces. Similarly, resolution of the in-plane forces for the *y*-aligned case shown in Figure 3 gives:

$$(T_{x1} + T_{x2} - T_{x4})\cos\gamma + (T_{y1} - T_{y3})\sin\gamma = C_1 - C_{y3}\sin\gamma + (C_{x2} - C_{x4})\cos\gamma \tag{4}$$

The basic movements of the facets are illustrated in Figure 4, which shows the rotations θ for the facets which rotate about the *y*-aligned edges, and ϕ for the facets which rotate about the *x*-aligned edges. Each facet also has a rigid-body movement (Δ_x or Δ_y) perpendicular to its supported edge. The origin of position coordinates is located at the top-right corner of the panel, on its top surface.

The general expression for horizontal *x*-movement at a point *(x, z)* on a facet rotating about an edge parallel to the *y*-axis, and particularly on a yield-line crack-face, is:

$$u = \Delta_x - \theta z - \frac{\theta^2 x}{2} \tag{5}$$

The horizontal *y*-movement at a point *(y, z)* on a facet rotating about an edge parallel to the *x*-axis is:

$$v = \Delta_y - \phi z - \frac{\phi^2 y}{2} \tag{6}$$

The optimal yield line pattern is determined by minimizing the load capacity over a range of yield line patterns defined by the value of n_x, at a vanishingly small deflection. In some cases a *y*-aligned yield line pattern is found to produce lower load capacities than any *x*-aligned pattern; this follows the slab aspect ratio when the reinforcing mesh is isotropic. Once the yield line pattern has been created, its alignment and position are fixed, and do not change as the deflection increases. The forces which appear in the horizontal equilibrium condition are the resultant compressions from the concrete stress blocks on the internal yield lines, together with the tensions in the *x* and *y* directions caused by the unfractured reinforcing bars which cross the yield lines. These are illustrated in Figures 2 and 3, which show the crack-surfaces of half of each of the facets for *x*- and *y*-aligned mechanisms.

At every increment of deflection it is necessary to satisfy one of the horizontal equilibrium Equations (3) or (4), the choice depending on the mechanism's alignment. However, the forces within the equation are calculated in different ways, depending on the concurrent condition of the compressive stress blocks and the bars crossing the yield lines:

- At zero deflection (Figure 5(a)) the stress blocks are of uniform depth ($z_1=z_2$). As the deflection increases z_2 decreases progressively, and rapidly becomes negative (Figure 5(b)), indicating that contact has been lost across the central yield line and an inner portion of the diagonal yield lines; the stress block is then triangular. At the panel corners the neutral axis depth z_1 initially increases, and may go below the level of the mesh ($z_1>\mu t$), as shown in Figure 5(c). In this analysis any mesh within a compressive zone is ignored. Under some circumstances the corner neutral axis depth can go below the lower surface of the slab ($z_1>t$), causing the stress block (Figure 5(d) to be trapezoidal.

- The mesh crossing the yield lines is initially entirely intact, but when the crack-width at the level of the bars in either direction exceeds the fracture crack-width then the corresponding bars fracture, as shown in Figures 5(c) and 5(d). The initial fracture is usually of all the *y*-direction bars crossing the central yield line simultaneously. At some point either the *x*- or *y*-direction bars crossing the diagonal yield lines begin to fracture from the yield-line intersection (a progressive "unzipping" effect), and this is followed by progressive fracture of the orthogonal bars. At large deflection the bars in either direction may be completely fractured across the diagonal yield lines. The exact form of either Equation (3) or (4) depends on the current stress block shape (Figure 5) and the rebar fracture state, and so in principle the forms need to be stated for all combinations of these, although for any particular set of details only a few of these cases will apply during the increase of deflection. In total 30 combinations exist for each of the *x*- and *y*-aligned mechanisms, and these are defined in Tables 1 and 5.

It is useful at this stage to write the different forms of Equations (3) and (4) in dimensionless terms, for which a set of dimensionless parameters is defined in the general Notation list. All the symbols which have until now been defined in units of distance are divided by the overall dimension l_y, and the mesh strengths per unit width are divided by $f_c l_y$. The key dimensionless parameters are for the corner neutral axis depth $\psi_1 = z_1 / l_y$ and the mesh strengths $\lambda_x = f_{px} / f_c l_y$ and $\lambda_y = f_{py} / f_c l_y$. The coefficients given in Tables 2-4 and 6-8 also use $\tau = t / l_y$ and the fracture crack-width parameters $\eta_x = \Delta_{\text{lim},x} / l_y$ and $\eta_y = \Delta_{\text{lim},y} / l_y$.

The form of Equation (3) for the small- (but finite) deflection condition denoted as *a1x* in Table 1, in which there are complete stress blocks on all yield lines and all rebar is intact, is written in these terms as:

$$\psi_1\left(n_x\left(\frac{1}{\sin\gamma\cos\gamma}+r-2n_x\right)+B_c\right)-\frac{n_x^2\theta}{2}\left(\frac{1}{2\sin\theta\cos\theta}+r-2n_x\right)+C_c-\frac{\lambda_x}{2}-\lambda_y r n_x+C_s=0 \qquad (7)$$

The corresponding horizontal equilibrium equations for each of the 30 *x*-aligned conditions are defined in the Appendix to this paper (Tables 2, 3 and 4), in which the coefficients of each term in a general quadratic form of an equation in ψ_1 are tabulated.

For *y*-aligned mechanisms the small-deflection condition a1y (Table 5) is written as:

$$\psi_1\left(\frac{r}{\sin\gamma\cos\gamma}+1-2n_y+B_c\right)-\frac{\theta r}{4}\left(\frac{r}{2\sin\gamma\cos\gamma}+1-2n_y\right)+C_c-\lambda_x-\frac{\lambda_y r^2}{2n_y}+C_s=0 \qquad (8)$$

The corresponding horizontal equilibrium equations for each of the 30 *y*-aligned conditions are defined in Tables 6, 7 and 8, again as the coefficients in a general quadratic form of an equation in ψ_1. At any deflection, defined by the value of θ, only one of the sets of 30 equations produces a value of ψ_1 which also gives the correct compression stress block and mesh fracture state.

2.2 Continuity terms

Equations (7) and (8) contain the terms B_c, C_c and C_s, which appear due to the presence of forces at the edges of the panel where there is continuity with adjacent panels, as shown in Figure 6. It has already been stated that only bi-symmetric continuity conditions will be considered in this paper, and also that two distinctly different forms of continuity can exist at panel edges. In the first of these the adjacent panels with which the panel under consideration are assumed continuous, but are allowed to move laterally so that no resultant forces are applied to the panel edges. In the second the lines of edge support are assumed to remain in their original positions, so that there is no rigid-body movement either of the

panel's edges or of any of the adjacent panels. These two cases can respectively be considered as having force-controlled and displacement-controlled boundary conditions.

2.2.1 Rotationally restrained edges

With rotationally restrained boundaries it is assumed that the external panels deflect in the same way as the panel under consideration, but that they can move horizontally outwards so that there is no net horizontal force crossing any edge of the slab. Any mesh tension across an edge is balanced by the compression in the concrete stress block (Figure 7(b) at the edge. If this mesh fractures, then external slabs move so that the edge compressive zone vanishes (Figure 7(c)). The neutral axis depth below the top surface of the slab is z_3 for the edge parallel to x, and z_4 for the edge parallel to y. With no net force across each edge then, for intact edge reinforcement, the neutral axis depths on the edges are given by:

$$t - z_3 = \frac{f_{py}}{f_c} \tag{9}$$

$$t - z_4 = \frac{f_{px}}{f_c} \tag{10}$$

In dimensionless terms these imply:

$$\psi_3 = \tau - \lambda_y \tag{11}$$

$$\psi_4 = \tau - \lambda_x \tag{12}$$

When the reinforcing bars crossing either edge fracture, then both the tension and compression forces across that edge vanish, and the neutral axis lies at, or beyond, the lower face of the slab.

The boundary forces are irrelevant to horizontal equilibrium, since they are always in balance for this boundary condition, and so the appropriate horizontal equilibrium equation, either (7) or (8), can be solved at any deflection value with the continuity terms B_c, C_c and C_s all set to zero. This does not imply that the edge forces play no part in either the initial yield-line failure load or the enhancement due to finite deflection, because their moments about axes along the slab edges clearly resist the rotations caused by the vertical deflection of the facets. It is convenient to express these forces using edge continuity flags k_{rx} and k_{ry} to specify whether these forces exist. Initially their values (1 for intact edge rebar, 0 for either no continuity or fractured rebar) depend on whether there is rotational continuity at the edges. Subsequently the fracture of reinforcement crossing either edge changes the value of the appropriate continuity flag to zero. Taking these continuity flags into account Equations (9) and (10) can be rewritten as:

$$z_3 = t - k_{ry}\frac{f_{py}}{f_c} \tag{13}$$

$$z_4 = t - k_{rx}\frac{f_{px}}{f_c} \tag{14}$$

It can be seen that z_3 and z_4 are constant for given f_{px}, f_{py} and f_c if rotational continuity is maintained, and are independent of the slab deformation, because the constant bar strength is always balanced by the same depth of compression block. When the reinforcement crossing an edge fractures the edge continuity flags vanish and z_3 and z_4 take the new constant value t.

The boundary forces are expressed as:

$$T_{x4} = k_{rx}\frac{f_{px}l_y}{2} \tag{15}$$

$$C_{x4} = T_{x4} \tag{16}$$

$$T_{y3} = k_{ry}\frac{f_{py}rl_y}{2} \tag{17}$$

$$C_{y3} = T_{y3} \tag{18}$$

The internal forces across the internal yield lines have previously been derived [27] for isolated panels, but it is worth re-stating them here.

$$C_1 = A_1 f_c \tag{19}$$

$$C_{y2} = A_{2y} f_c \quad \text{or} \quad C_{y2} = 0 \tag{20}$$

$$T_{y1} = \left(x_{lim,1y} - x_{t,1}\right) f_{py} \tag{21}$$

$$T_{x1} = \left(y_{lim,1x} - y_{t,1}\right) f_{px} \tag{22}$$

$$T_{y2} = \left(r/2 - n_x\right) l f_{py} \quad \text{or} \quad T_{y2} = 0 \tag{23}$$

2.2.2 Axially restrained edges

If pairs of parallel edges to the panel are constrained against rigid-body movement, so that the adjacent panels can rotate about the edges and form similar mechanisms without any resultant horizontal movement, then this situation with either intact or fractured reinforcement is illustrated in Figures 7(e) and 7(f). In this case the position of the neutral axis is displacement-controlled, and the edge compression and tension forces follow from this. This results in a much larger compression block than in the previous case, generating a large compressive force that resists the rotation of the facets. The compressive force usually greatly exceeds the tensile force induced by the reinforcement mesh, creating an "arching'' action in the slab between this compressive edge reaction in the lower part of the slab cross-section and the compressive forces in the upper part of the cross-section across the internal yield lines. This has the capacity to increase the load capacity greatly, at least at small deflections.

The neutral axis depths at the panel edges are:

$$z_3 = \frac{\Delta_y}{\phi} = z_1 \tag{24}$$

$$z_4 = \frac{\Delta_x}{\theta} = z_1 \tag{25}$$

Once again, continuity flags are used to distinguish between the possible conditions at the panel edges. The rebar continuity flags krx and kry can be set to 1 for intact edge rebar, or to 0 if there is no rebar continuity or the rebar has been fractured. For this case the additional continuity flags kcx and kcy are set to 1 for concrete restraint, or zero if the concrete contact zone can move perpendicular to the edge. Using both of these continuity flags at each edge allows the continuity terms B_c, C_c and C_s to be expressed in a unified fashion for the horizontal equilibrium equations.

The boundary forces are expressed as:

$$C_{x4} = k_{ax} \frac{f_c l_y (t - z_4)}{2} \tag{26}$$

$$T_{x4} = k_{rx} \frac{f_{px} l_y}{2} \quad \text{if } z_1 > \mu t \tag{27}$$

$$C_{y3} = k_{ay} \frac{f_c r l_y (t - z_3)}{2} \tag{28}$$

$$T_{y3} = k_{ry} \frac{f_{py} r l_y}{2} \quad \text{if } z_1 > \mu t \tag{29}$$

With respect to Equations (27) and (29), the edge rebar forces are consistent with the general rule in this methodology, that rebar forces which lie within a compression zone are discounted. Hence:

$$T_{x4} = 0 \text{ if } z_1 < \mu t \tag{30}$$

$$T_{y3} = 0 \text{ if } z_1 < \mu t \tag{31}$$

Since the neutral axis depth at any deflection is mainly controlled by the boundary restraint to horizontal movement, and the slab is lightly reinforced, the neutral axis will in general lie in the vicinity of the mid-depth of the slab. At infinitesimal and small deflections the mesh level within the slab will therefore lie within the concrete stress block, either across the slab edges or across the internal yield lines, but never within both of these. At larger deflections the neutral axis depth (z_2) at the yield line intersections will reduce, and the neutral axis will rise above the mesh level in the central region of the slab. However, the initial horizontal equilibrium case may be either a1x/a1y for mesh placed relatively low in the cross-section or a2x/a2y for mesh placed relatively high. This contrasts strongly with the initial behaviour of panels without axial edge restraint, for which the initial case is usually a1x/a1y.

2.3 Transverse equilibrium and load capacity

Vertical equilibrium, and hence the load capacity of the composite panel at high deflections, can easily be established by equating the external (load-induced) and internal moments within each of the two types of facet about their supported edges. There are equal and opposite resultant transverse shear forces between these facets at each of the diagonal yield lines, which do not affect the horizontal equilibrium equations given in Section 3.4. It is assumed for convenience (although it is irrelevant to the eventual solution) that these transverse shear forces act through the centroid of the concrete stress-block on the diagonal yield line. Because of the inherent symmetry there is no transverse shear force crossing the central yield line. The forces involved in the internal and external moments about the edge axis XX' for

an *x*-aligned trapezoidal facet are shown in Figure 8(b) and about YY' for the corresponding triangular facet in Figure 8(a).

2.3.1 *x*-aligned mechanism

For an *x*-aligned mechanism the equivalent equations for the triangular facet about YY' are:

$$M_{Tx1} = T_{x1}\left((x_{\lim,1x} + x_{T,1})\frac{\theta}{2} - t(1-\mu)(1-\frac{\theta^2}{2}) \right) \tag{32}$$

$$M_{CS} = (C_1 \cos\gamma_x - S\sin\gamma_x)\left(-x_{CA1}\theta + (t - z_{CA1})(1-\frac{\theta^2}{2}) \right) \tag{33}$$

$$M_V = V\left((t - z_{CA1})\theta + x_{CA1}(1-\frac{\theta^2}{2}) \right) \tag{34}$$

The complete "internal" moment is then:

$$M_{\text{int}} = M_{Tx1} + M_{CS} + M_V \tag{35}$$

The external moment about YY' for this facet is:

$$M_{Ext} = \frac{pn_x l_y^2}{4}\left(t\theta + \frac{n_x l_y}{3}(1-\frac{\theta^2}{2}) \right) \tag{36}$$

For the trapezoidal facet the corresponding internal moment equations about XX' are:

$$M'_{Ty1} = T_{y1}\left((y_{\lim,1x} + y_{T,1})\frac{\phi}{2} - t(1-\mu)(1-\frac{\phi^2}{2}) \right) \tag{37}$$

$$M'_{Ty2} = T_{y1}\left(l_y\frac{\phi}{2} - t(1-\mu)(1-\frac{\phi^2}{2}) \right) \tag{38}$$

$$M'_{CS} = -(C_1 \sin\gamma_y + S\cos\gamma_y)\left(y_{CA1}\phi - (t - z_{CA1})(1-\frac{\phi^2}{2}) \right) \tag{39}$$

$$M'_{Cy2} = -C_{y2}\left(l_y \frac{\phi}{2} - (t - \frac{z_2}{2})(1 - \frac{\phi^2}{2}) \right) \tag{40}$$

$$M'_V = -V\left((t - z_{CA1})\phi + y_{CA1}(1 - \frac{\phi^2}{2}) \right) \tag{41}$$

So that

$$M'_{\text{int}} = M'_{Ty1} + M'_{Ty2} + M'_{CS} + M'_{Cy2} + M'_V \tag{42}$$

The "external" moment about XX' is:

$$M'_{Ext} = \frac{pl_y^2}{2}\left((\frac{r}{2} - n_x)\left(t\phi + \frac{l_y}{4}(1 - \frac{\phi^2}{2}) \right) + \frac{n_x}{2}\left(t\phi + \frac{l_y}{6}(1 - \frac{\phi^2}{2}) \right) \right) \tag{43}$$

The transverse shear force can be eliminated from these equations if Equations (42) and (43) are each multiplied by the factor $(-M_V / M'_V)$ and respectively added to Equations (35) and (36). The transverse equilibrium equation is then:

$$M_{Ext} - (M_V / M'_V)M'_{Ext} = (M_{Tx1} + M_{CS}) - (M_V / M'_V)(M'_{Ty1} + M'_{Ty2} + M'_{CS} + M'_{Cy2}) \tag{44}$$

2.3.2 *y*-aligned mechanism

The equilibrium equation for a *y*-aligned trapezoidal facet can be aggregated from the individual internal moments, equated to the opposing external moments. The bottom edge of the concrete slab is selected as the level for the axes XX' and YY' about which these moments are calculated. The "internal" clockwise moments about YY' are:

$$M_{Tx1} = T_{x1}\left((x_{\text{lim},1x} + x_{T,1})\frac{\theta}{2} - t(1 - \mu)(1 - \frac{\theta^2}{2}) \right) \tag{45}$$

$$M_{Tx2} = T_{x2}\left(rl_y \frac{\theta}{2} - t(1 - \mu)(1 - \frac{\theta^2}{2}) \right) \tag{46}$$

$$M_{CS} = (C_1 \cos\gamma_y + S\sin\gamma_y)\left(-x_{CA1}\theta + (t - z_{CA1})(1 - \frac{\theta^2}{2})\right) \tag{47}$$

$$M_{Cx2} = C_{x2}\left(-rl_y\frac{\theta}{2} + (t - \frac{z_2}{2})(1 - \frac{\theta^2}{2})\right) \tag{48}$$

$$M_V = V\left(-(t - z_{CA1})\theta - x_{CA1}(1 - \frac{\theta^2}{2})\right) \tag{49}$$

The complete "internal" moment is then:

$$M_{\text{int}} = M_{Tx1} + M_{Tx2} + M_{CS} + M_{Cx2} + M_V \tag{50}$$

The "external" moment about YY' is:

$$M_{Ext} = \frac{prl_y^2}{2}\left(\frac{n_y}{2}\left(t\theta + \frac{rl_y}{6}(1 - \frac{\theta^2}{2})\right) + (\frac{1}{2} - n_y)\left(t\theta + \frac{rl_y}{4}(1 - \frac{\theta^2}{2})\right)\right) \tag{51}$$

For the corresponding triangular facet the "internal" clockwise moments about XX' are:

$$M'_{Ty1} = T_{y1}\left((y_{\text{lim},1x} + y_{T,1})\frac{\phi}{2} - t(1-\mu)(1 - \frac{\phi^2}{2})\right) \tag{52}$$

$$M'_{CS} = -(C_1 \sin\gamma_y - S\cos\gamma_y)\left(y_{CA1}\phi - (t - z_{CA1})(1 - \frac{\phi^2}{2})\right) \tag{53}$$

$$M'_V = V\left((t - z_{CA1})\phi + y_{CA1}(1 - \frac{\phi^2}{2})\right) \tag{54}$$

The internal moment for the triangular facet about XX' is therefore:

$$M'_{\text{int}} = M'_{Ty1} + M'_{CS} + M'_V \tag{55}$$

The external moment for the triangular facet about XX' is:

$$M'_{Ext} = \frac{prn_y l_y^2}{4}\left(t\phi + \frac{n_y l_y}{3}(1 - \frac{\phi^2}{2}) \right) \tag{56}$$

Again, the transverse shear force can be eliminated from these equations if Equations (55) and (56) are each multiplied by the factor $(-M_V / M'_V)$ and respectively added to Equations (50) and (51). The transverse equilibrium equation is then:

$$M_{Ext} - (M_V / M'_V)M'_{Ext} = (M_{Tx1} + M_{Tx2} + M_{CS} + M_{Cx2}) - (M_V / M'_V)(M'_{Ty1} + M'_{CS}) \tag{57}$$

This gives the enhanced value of the applied load for a case in which the steel temperature is kept constant.

3. Application of the models

The method has previously been tested [27] against the current methods [18, 19, 21, 22], which are all based on the work of Hayes [14]. This has shown that the enhancement of load capacity with deflection differs from predictions given by these methods. There is also the major difference that mesh will fracture abruptly along yield lines orthogonal to the edges of the slab, as well as progressively along diagonal yield lines, both of which can cause the enhancement to be lost. The current methods only deal with isolated panels without continuity across their edges, and so there can be no similar comparisons for cases with edge continuity. It is, however, possible to use the new development to compare the effects of different parameters, including the fracture ductility of reinforcement, on the predicted behaviour.

The ductility to fracture of the mesh is most conveniently defined as the length to which it can be stretched between the intact concrete faces of a discrete crack before fracturing. Numerical values for fracture crack-width have been postulated, for standard reinforcement ductility grades and for both deformed and plain bar reinforcement, in the previous paper [28]. The basic method for modelling the bond between the bars and concrete on either side of a discrete crack was set out by Sezen and Setzler [29] based on experimental testing, and involves dividing the anchorage length behind the crack-face into elastic and plastic zones, each with a constant bond strength. These bond strengths were roughly characterized using results from several researchers, so that the bar forces at the welds connecting orthogonal bars can be calculated. These welds are assumed to fracture when the bar force is above half its own strength, and the bar strain can reduce with distance into the concrete until it naturally becomes zero; otherwise these weld positions to transverse bars form solid anchorages beyond which there is no bar strain or bond stress. Standard reinforcing meshes [30] have three ductility classes, of which Class A has very low ductility,

Class B has moderate ductility and Class C has high ductility. It is common current practice to use mesh of Class B with a deformed profile in order to maximize bond to the surrounding concrete; this is considerably higher than can be achieved with plain prismatic bars. Table 9 shows the fracture crack-widths given by the method for isotropic meshes consisting of both plain and deformed bars of 6 mm to 12 mm diameter and ductility classes B and C, at 200 mm spacing.

3.1 The effects of rotational continuity

The well-documented Garston test conducted by Bailey [31] at BRE, Garston, was an ambient-temperature slab test intended to simulate the behaviour of a Cardington corner bay at the stage when its central attached unprotected downstand steel beam had lost nearly all of its strength at very high temperatures. The Garston test panel was 9500 mm x 6460 mm in overall dimensions (aspect ratio 1.4706), and 120 mm thick. It had an A142 smooth mesh (isotropic with 6 mm bars at 200 mm spacings) placed at a 69mm effective depth. The concrete had compressive strength of 52 MPa, recorded at the time of the test, and the mesh had a tensile strength of 580 MPa with fracture strain of 0.12. For this analysis the steel ultimate strength is assumed to be 500 MPa. The slab panel was laterally unrestrained, and had no continuity across its edges. This test was used [27] to compare the predictions of the current method with those from the method developed by Bailey and Moore [18, 19]. This test is also useful in doing some basic studies on the effect of edge continuity.

The effect of rotational continuity at edges that are free to move horizontally is illustrated in Figures 9 and 10. For a "Garston" slab the effects of mesh fracture at the edges and across the internal yield lines are illustrated in Figures 9(a and b) which respectively show the progression of load capacity with deflection for a panel with rotational continuity across all edges, and for a panel with no edge continuity. In both cases the fracture crack-width is set at 5.43mm, which represents the behaviour of plain A142 mesh of ductility Class B. In these cases the mean effective depth of the mesh has been set at 30mm to emphasize the role of the edge continuity.

It can be seen that the initial effect of edge continuity is to increase the small-deflection yield-line load capacity; with a low effective depth the increase of capacity from discontinuous to continuous at the edges is over four times. In Figure 9(a) sudden fracture of the edge bars across the long edge causes a drop in load capacity; this is followed shortly by fracture of short-edge bars, together with the bars crossing the middle yield line, which causes another instantaneous drop in capacity. A progressive loss of capacity starts to happen when bars crossing the diagonal yield lines begin to fracture ("unzip"); this continues, with further loss of capacity, until all these bars are fractured. For the discontinuous slab, in Figure 9(b) the process has only a single instantaneous loss of capacity, when the central yield line mesh fractures, and the peak capacity occurs with the start of "unzipping" at the diagonal yield lines.

Figure 10 shows the same test applied to a square panel of side length 6460 mm, again with the material and reinforcing characteristics of the Garston test slab. It is clear that the enhancement of capacity due to TMA is most effective for the square configuration. For bi-symmetric edge conditions there is no central yield line, and so there is no abrupt loss of capacity due to fracture of the mesh across this yield line, although it does happen for the two mono-symmetric cases, which generate a central yield line.

A comparison of the enhancement characteristics for slabs with different mesh effective depths and the full range of rotational continuity conditions is shown in Figure 11.

In the left-hand column of graphs (Figures 10(a, c, e)) the mesh is of the intermediate Ductility Class B and the bars are plain rather than deformed; this gives a fracture crack-width of 5.43 mm. In the right-hand column (Figures 10(b, d, f)) the mesh is again plain and of the highest Ductility Class C, giving a fracture crack-width of 11.08 mm. Graphs are shown for different mean effective depths of the mesh; Figures 10(a, b) are for 30mm, and Figures 10(e, f) are for 90mm. Figures 10(c, d) are for 69mm, which was the actual effective depth in the "Garston" test. Within each graph four cases of edge continuity are plotted. In their initial states the four cases have: (i) no continuity ($k_{rx} = k_{ry} = 0$); (ii) and (iii) continuity across one set of parallel edges only ($k_{rx} = 1$, $k_{ry} = 0$ or $k_{rx} = 0$, $k_{ry} = 1$); (iv) continuity across all edges ($k_{rx} = k_{ry} = 1$). This figure shows the effect of fracture crack-width, which is determined by the mesh ductility class and bar surface type. The most evident effect of an increased fracture crack-width is that the peak enhancement of load capacity is increased, and occurs at a higher displacement. This peak capacity occurs when the mesh begins to "unzip" along the diagonal yield lines. The abrupt reductions in capacity occur when mesh crossing the yield lines along and parallel to the panel's edges fractures simultaneously. It can be seen that continuity affects mainly the initial yield-line capacity, which increases with the length of the panel boundary that is continuous. The subsequent enhancement of this capacity due to TMA is initially very similar for all of the different edge conditions.

3.2 Continuity of slabs with fixed edges

When the edges of a panel are restrained against outward movement, then the effect of the concrete "hogging" stress blocks created around the restrained edges is to cause a very large increase of the initial yield-line load capacity above the capacity of either simply supported or rotationally continuous edge conditions. This effect is compressive membrane action (CMA), and is effectively a 2-dimensional arching effect, caused by resultant compressive forces in the lower part of the cross-section around the slab edges in combination with resultant compressive forces in the upper part of the cross-section in the central part of the slab. Since the key aspect of this mechanism is the lever-arm between these resultant forces it is logical that, as the slab deflects, this lever-arm decreases and the load capacity of the slab falls. At some stage of deflection, if the mesh has not fractured, it is possible that TMA will develop.

3.2.1 Comparison of the new method of CMA with Wood's Test FS12

Wood [6] carried out a series of tests on reduced-scale slab panels, some of which were cast together with substantial surrounding ring-beams which were then clamped down. This surround had sufficient stiffness and strength to constitute a very credible model of continuity within the inner panels of a continuous concrete floor, vertically supported on a square grid. His Test FS12 is described in detail, and is used for comparison here.

The square slab denoted as FS12 was supported by the reinforced surround mentioned above, which was intended to prevent rotation, vertical movement and spreading. It was equally loaded at 16 points to represent uniformly distributed loading, using a cable system. The tested slab had dimensions 1727.2 mm x 1727.2mm, with thickness 57.2 mm, as shown in Figure 12(b). The slab was under-reinforced, with a single layer of isotropic mesh with 4.8 mm bar diameter of and 146.1 mm bar spacing, placed at a mean 46 mm depth in the slab. The cube strength of the concrete was 40.7 MPa, corresponding to 32.5 MPa cylinder strength; the well-defined strength of the steel mesh was 233 MPa. It is assumed that the bars used had a plain (undeformed) profile, although this is not specifically documented. Wood describes this test in detail, mainly because of the unexpectedly high load which it sustained before failing suddenly at an applied load intensity of 116.3 kN/m^2. The dynamic nature of the failure caused such rapid damage to the concrete that the test was stopped by removing the load; the damaged specimen was later re-loaded. These two parts of the test record are shown in Figure 12.

Predictions of the new procedure, making three different assumptions for the mesh ductility, are also included on this figure. Meshes with fracture crack-widths of 1.01 mm (approximately equivalent to deformed mesh of Ductility Class B in these conditions) and 5.43 mm (equivalent to plain mesh of Ductility Class B; the assumed mesh), as well as a mesh with effectively infinite ductility, are plotted on Figure 12. The initial observation from this figure is that the initial peak failure load of 182.5 kN, given by the current approach, lies very close to Wood's prediction of 178.9 kN, based on a uniform enhancement of the yield-line moment capacity by membrane force. This can be rationalized by remembering that at zero deflection the concrete stress blocks on all the yield lines are of uniform depth, and so the plastic moment per unit length is uniform, so a uniformly enhanced plastic moment would be appropriate. At finite deflection Wood gives no prediction that is based on a square slab.

In comparing the test and theoretical results it should be remembered that the test results show the complete test record, including the elastic and partially-plastic ranges of load and deflection, whereas the theoretical curves represent rigid-plastic load capacity as a function of deflection. All deflections contribute to the reduction of the lever-arm referred-to above, and so it is impossible for the initial peak capacity to reach the theoretical rigid-plastic value. It is also clear that the surrounding frame in Wood's test must have had a finite flexibility, which would increase the extent of the elastic range of deflection above that which it would have experienced if the restraint had been provided by a floor with continuity beyond all edges of the slab panel. An indication of how the peak capacity would actually be reduced

during the elastic and elasto-plastic phases is shown. Eyre [32] logically suggested that, in order to be able to calculate realistic peak load capacities in CMA, it will be necessary to research the equivalent horizontal elastic restraint stiffnesses at the edges of slabs in terms of their location within a floor. In the case of Wood's test this would largely depend on the characteristics of the supporting frame, whereas in the central zone of a large continuous concrete floor it would depend mainly on the internal axial stiffness properties of the individual slab panel itself.

Within the deflection range plotted on Figure 12 it is seen that the infinite-ductility theoretical plot just starts to rise progressively as TMA begins to dominate the load capacity. This is explored in more detail in Section 3.2.4. In the two more practical cases of fracture crack-widths, the fracture of reinforcement prevents any tendency for the load capacity to rise, and in fact both curves reach zero at approximately 400 mm deflection. This is examined further in Section 3.2.3.

3.2.2 Variation of load capacity under different continuity conditions of fixed boundaries

It is worth briefly examining the effects of the events, such as fracture of bars across yield lines and the alignments of the neutral axes on the yield lines. The "Garston" test slab specification defined previously is again used for this purpose. Two different mesh ductilities are compared in Figure 13; an effectively infinitely ductile mesh which has no relevant fracture crack-width, and the most ductile practical plain mesh (of Ductility Grade C), which has 11.08 mm fracture crack-width. Complete edge continuity is assumed, with mesh continuous across all edges, and restraint to movement at all edges.

The general trends of behaviour differ greatly, depending on the mesh ductility. If the mesh has sufficient ductility to remain intact across the yield lines (Figure 13(a)) then the only notable events concern the change of neutral axis alignment. At zero deflection this is initially horizontal on all yield lines, which reflects the normal assumption for linear yield-line theory. As the deflection grows the neutral axis on the diagonal yield lines rotates. The first event of note is when its level at the slab corners falls below the effective depth of the mesh; the second occurs when its position along the central yield line rises above the slab's upper surface. This is equivalent to a complete separation of the crack surfaces along this yield line, and the start of progressive separation along the diagonal yield lines. Since no mesh fracture occurs, further deflection induces TMA, which progressively enhances the load capacity. For the case shown in Figure 13(b), in which the mesh has a fracture crack-width of 11.08 mm, these stages are followed by a series of events due to bar fracture, each of which reduces the load capacity. Of these, the abrupt changes to load capacity are those where all the bars crossing the central yield line, and later the slab edges, fracture simultaneously. Progressive fracture ("unzipping") of the *x*- and *y*-aligned bars crossing the diagonal yield lines, which each cause increases of the downward gradient of the curve, occur between these abrupt fractures. The resulting curve gives no evidence of enhancement of capacity due to TMA, and the load capacity continues to decrease towards zero.

Figure 14 shows the effect of edge constraints on the load capacity variation with deflection for different mesh ductilities. In each case the mesh is continuous across the slab edges. In each of the graphs cases are shown for edge restraint on: all edges; the long (x-aligned) edges; the short (y-aligned) edges. The fourth case on each graph has no edge restraint. The mesh ductility is identical within each graph, represented as fracture crack-widths: (a) effectively infinite; (b) 11.08 mm; (c) 5.43 mm; (d) 1.01 mm.

In each graph the initial yield-line capacities are identical, and logically in the order of the restrained perimeter lengths. The cases with restrained short-span edges produce a y-aligned mechanism, whereas all the three other restraint cases produce x-aligned mechanisms. This explains why the shapes of the curves for restrained short-span edges appear different from (and in fact cross) the other curves.

3.2.3 The influence of mesh size on load capacity enhancement

Apart from the comparison with Wood's test, the previous analyses have assumed a very low reinforcement ratio, based on a single layer of isotropic A142 mesh, consisting of 6 mm bars at 200 mm spacing. In the 120 mm thick slab used in the Garston test this represents a reinforcement ratio of 0.118%. Even with a non-standard isotropic mesh of 12 mm bars at 200 mm spacings the reinforcement ratio in either direction is below 0.5%, so the yield lines should still be discrete. In Figure 15 the effect of mesh size on the slab's transition from CMA to TMA, provided that there is no prospect of bar fracture, is illustrated.

The figure shows load capacity as a function of deflection for panels of the "Garston" specifications, including a mean mesh effective depth of 69 mm, for isotropic meshes of 6 mm, 8 mm, 10 mm and 12 mm bars at 200 mm spacing. In each case two variations are shown, one of which has restraint to movement on all edges as well as continuity of reinforcement; these are shown as black curves. The other case, shown in red, has no restraint to in-plane movement although it has continuity of reinforcement. The restrained cases initially exhibit CMA, with a load capacity which reduces with deflection. It is notable that the mesh size has virtually no effect on the initial capacity, but does affect the rate at which the strength is lost. The more significant effect of the mesh size is in influencing the growth of TMA; the load capacity growth for 12 mm mesh is much higher, and at lower deflections, than that for 6 mm mesh. Within each pair of cases the curves cross at some point, so that the capacity in TMA is higher for the unrestrained case, although the initial (CMA) capacity is much higher for the restrained case. Although superficially it might be assumed that the two curves would converge at very high deflection, actually the edge forces are completely different in the two cases, and the compressive edge forces in the restrained case reach a stage at which their effect is to increase deflections. The curve linking the crossover points is marked on the figure.

3.2.4 The influence of mesh fracture crack-width

The effect of the mesh ductility, defined as a fracture crack-width, has already been seen to be crucial to the load capacity variation with slab deflection. Using the Garston test specification again, the behaviour of horizontally restrained slabs which only differ with respect to their fracture crack-widths is illustrated clearly in Figure 16.

It is clear that TMA cannot be generated after CMA unless intact mesh can be retained across the yield lines up to high deflections. The meshes with lowest ductility (2 mm and 10 mm fracture crack-width) exhibit continuously falling load capacity as the deflection increases. The other finite ductilities (up to 100 mm fracture crack-width) show a falling capacity which then increases from a minimum until mesh fracture occurs.

4. CONCLUSION

The approach to large-deflection limit-state behaviour of slabs outlined in this paper relies on the assumptions underpinning yield line analysis holding good. In particular it is assumed that a pattern of discrete yield lines forms, and that this pattern does not change as deflections increase. In order to ensure that this assumption is generally valid, the method is assumed to apply to thin lightly reinforced slabs with a single layer of isotropic reinforcing mesh, and the examples presented all assume a steel area in either direction which is considerably less than 1% of the gross cross-sectional area. It does not attempt to model the failure mechanisms for thick, or highly reinforced slabs, for which flexural behaviour may not be the critical failure mode. Hence it does not attempt to include shear failure.

Within this context, the general philosophy has been to use a correct representation of the kinematics and equilibrium of the flat facets separated by the yield lines. For a slab which is unrestrained against horizontal movement at its edges, even if its reinforcement is continuous, the initial yield line failure load is increased by tensile membrane action as the deflection rises. If restraint to horizontal movement is present at the slab edges then compressive membrane action is induced; the initial failure load is very much higher, but falls as deflection increases. The most significant observation to be made about results produced by the methodology developed in this paper concerns the relative influences of concrete and reinforcing mesh on these two mechanisms. The initial load capacity in CMA is almost independent of the quantity or strength of the mesh, whereas the initial yield line capacity in TMA is controlled mainly by fracture of the mesh. The most radical difference between the approach of the authors and those of previous investigations into the enhancement of yield-line capacity at finite deflections lies in the assumption that, at a certain crack opening width, a rebar will fracture. This fracture crack-width is the essential measure of ductility that controls the behaviour. This ductility is increased by using bar profiles with low bond to the concrete (such as plain bars) and by using bars of a grade which is inherently ductile; it is decreased by using bars with deformed profiles, giving high bond strength, and by using less ductile material grades. It seems clear that the range of deflection within which tensile membrane action can

cause a significant enhancement of load, either above its yield line capacity or above a minimum after initial CMA, is restricted by the low fracture crack-widths which result from the use of deformed reinforcing bars. It may seem counter-intuitive to structural designers that well-bonded reinforcement gives the least effective deflection-induced enhancement in TMA; the general theme in normal design is that high bond is advantageous, and deformed-profile reinforcement is the norm in reinforced concrete construction. However, in specialized cases where large deflections are acceptable, generally where the avoidance of disproportionate collapse in extreme loading conditions is the priority, it is clear that increasing the fracture crack-width of reinforcement is the key strategy. This is true either in cases where there is no restraint to outward movement, in which a simple yield-line failure load is subject to increased deflection, or in cases where edge restraint causes early-stage CMA, with the possibility of enhanced capacity due to TMA at higher deflections. It seems obvious that deformed bars are unlikely to provide the ductility required to mobilize TMA, but that plain bars welded to orthogonal bars at spacings rather longer than the 200 mm used in the standard meshes considered in this paper may give sufficient ductility. An alternative in such cases would be to use bars with a plain profile but positive end-anchorage, for which the very long gauge-length would create very high fracture crack-widths. With this design specification, designers should also be able to quantify fracture crack-widths with much more confidence than is possible for continuously bonded bars. It should be remembered that tensile membrane action is considered as a viable design strategy against extreme "hazard" loading scenarios such as fire [18, 19] or sudden column removal due to explosion [33], rather than in routine limit state design.

In real terms, it is obvious that, for "internal" panels, the sharp cusp shown on every CMA curve of load capacity against deflection is caused by the infinite stiffness represented by the edge restraint condition against outward movement which has been assumed. Even in terms of a model based on an assembly of flat facets, there is some elastic stiffness associated with restraint to outward movement at every edge of the slab, at least in the initial range of deflection. This represents the elastic strain components associated with the concrete stress blocks; a similar effect occurs at each internal yield line. In cases where two opposing edges are modelled as free to move there may also be some elastic stiffness representing restraint from edge beams and columns in the real structure. Any such finite stiffness, replacing the absolute restraint currently assumed, will produce continuous curves of load capacity against deflection which show limits to load capacity which are lowered from the sharp cusp of the idealized curve. Eyre [32] commented about the necessity to attempt to quantify edge stiffness, although in the context of a very different approach to CMA. It should also be noted that this stiffness would be an uncoupled ("Winkler") representation of the real continuum effect. A further extension of the approach may be to represent the brittle nature of the concrete stress-strain curve by including a negative post-peak-strength stiffness in the representation of the concrete stress blocks. Even without an attempt to quantify these effective stiffnesses, this development is a significant one, and will be undertaken as an extension to the model.

This work is a "spin-off" from studies aimed at rationalising the observed enhancement of the fire resistance of composite slab panels by tensile membrane action. Because of the very large double curvatures caused by rapid heating of the downstand steel beams, the concrete slabs naturally generate a tensile membrane action which increasingly becomes the dominant load-carrying mechanism as the steel temperature rises. Thin, lightly-reinforced slabs have been considered, because these are characteristic of such slab panels. The initial studies [27] considered the enhancement of yield-line load-capacity of plain simply supported concrete slabs at ambient temperature as a function of deflection, and these formed the basis for further studies [28] in which the loading of a simply supported composite panel remained constant while the temperatures of its downstand beams were increased. It is considered necessary to understand the essential load-carrying mechanics of TMA, as well as specializing the investigation to the fire case, and hence this study, in common with the initial study [27], has considered the basic ambient-temperature case. In further work, one significant extension will be an investigation of the effects of continuity of slab panels on their behaviour in fire conditions.

REFERENCES

[1] Westergaard, H.M. and Slater, W.A., ' Moments and stresses in slabs', Proc. American Concrete Institute, 17 (1921), pp 415–538.

[2] Ockleston, A.J., 'Load tests on a three storey building in Johannesburg', The Structural Engineer, 33, (1955), pp 304 -322.

[3] Ockleston, A.J., 'Arching action in reinforced concrete slabs', The Structural Engineer, 36 (6), (1958), pp 197–201.

[4] Park, R., 'Ultimate strength of rectangular concrete slabs under short-term uniform loading with edges restrained against lateral movement', Proceedings Instn. Civ. Engrs, 28, (1964) pp 125-150.

[5] Park, R., 'The lateral stiffness and strength required to ensure membrane action at the ultimate load of a reinforced concrete slab and beam floor', Magazine of Concrete Research, 17 (50), (1965), pp 29-38.

[6] Wood, R.H., 'Plastic and elastic design of slabs and plates, with particular reference to reinforced concrete floor slabs', Thames and Hudson, London, (1961).

[7] Christiansen, K.P., 'The effect of membrane stresses on the ultimate strength of an interior panel in a reinforced concrete slab', The Structural Engineer, 41(8), (1963), pp 261–265.

[8] Johansen, K.W., 'Yield-line theory', Cement and Concrete Association, London, (1962).

[9] Park, R. and Gamble, W.L., 'Reinforced concrete slabs', Wiley Interscience, 2nd Ed. New York, (2000), pp 636- 694.

[10] Kirkpatrick, J., Rankin, G.I.B. and Long, A.E., 'Strength evaluation of M-beam bridge deck slabs', The Structural Engineer, 62B, (3), (1984) pp 60-68.

[11] Kuang, J. S. and Morley, C. T., 'A plasticity model for the punching shear of laterally restrained concrete slabs with compressive membrane action', International Journal of Science, 35, (5), (1993) pp 371-385.

[12] Sawczuk, A. and Winnicki, L., 'Plastic behavior of simply supported reinforced concrete plates at moderately large deflections', Int. J. Solids Structures, 1, (1965), pp 97-111.

[13] Kemp, K.O., 'Yield of a square reinforced concrete slab on simple supports, allowing for membrane forces', The Structural Engineer, 45 (7), (1967), pp 235-240.

[14] Hayes, B., 'A study of the design of reinforced concrete slab structures', PhD thesis, University of Manchester, (1968), 398pp.

[15] Taylor R. (1965), 'A note on a possible basis for a new method of ultimate load design of reinforced concrete slabs', Magazine of Concrete Research, 17 (53), (1965) pp183–6.

[16] Kirby, B.R., 'The behaviour of multi-storey steel framed buildings in fire: a European joint research programme', British Steel Swinden Technology Centre, (1999).

[17] Newman G.M., Robinson J.T. and Bailey C.G., 'Fire safe design: A new approach to multi-storey steel-framed buildings', The Steel Construction Institute, Ascot, UK (2000).

[18] Bailey, C.G. and Moore, D.B., 'The structural behaviour of steel frames with composite floors slabs subject to fire – Part 1: Theory', The Structural Engineer, 78 (11), (2000), pp 19-27.

[19] Bailey, C.G. and Moore, D.B., 'The structural behaviour of steel frames with composite floors slabs subject to fire – Part 2: Design', The Structural Engineer, 78 (11), (2000), pp 28-33.

[20] Clifton, G.C. and C. Beck, Design of multi-storey steel framed buildings with unprotected secondary beams or joists for dependable inelastic response in fires: Second Edition. Steel Design and Construction Bulletin, 71, (2003), pp 3 - 72.

[21] Vassart, O. and Zhao, B., 'FRACOF: Fire resistance assessment of partially protected composite floors. Design guide', Arcelor Mittal & CTICM, (2011).

[22] Vassart, O. and Zhao, B., 'FRACOF: Fire resistance assessment of partially protected composite floors. Engineering background', Arcelor Mittal & CTICM, (2011).

[23] Foster, S.J., Bailey, C.G., Burgess, I.W. and Plank, R.J., 'Experimental Behaviour of Concrete Floor Slabs at Large Displacements', Engineering Structures, 26 (9), (2004) pp 1231-1247.

[24] Bailey, C.G. and Toh, W.S., 'Small-scale concrete slab tests at ambient and elevated temperatures', Engineering Structures, 29, (2007), pp 2775–2791.

[25] Lim, L. and Wade, C., 'Experimental fire tests of two-way concrete slabs', Fire Engineering Research Report 02/12. University of Canterbury and BRANZ Ltd, New Zealand, 2002.

[26] Lim, L., Buchanan, A., Moss, P. and Franssen, J.-M., 'Numerical modelling of two-way reinforced concrete slabs in fire', Engineering Structures, 26, (2004), pp 1081–1091.

[27] Burgess I.W., 'Yield-line plasticity and tensile membrane action in lightly-reinforced rectangular concrete slabs', Engineering Structures, 138, (2017), pp 195-214.

[28] Burgess, I.W. and Sahin, M., 'Tensile membrane action of lightly-reinforced rectangular composite slabs in fire', Structures, 16 (2018) pp. 176–197.

[29] Sezen, H. and Setzler, E.J., 'Reinforcement slip in reinforced concrete columns', ACI Structural Journal, 105 (3), (2008) pp 280–289.

[30] 'BS 4483:2005: Steel fabric for the reinforcement of concrete. Specification', British Standards Institution, London, (2005).

[31] Bailey, C.G., 'Membrane action of unrestrained lightly reinforced concrete slabs at large displacements', Engineering Structures, 23, (2001) pp 470-483.

[32] Eyre, J.R., 'Direct assessment of safe strengths of RC slabs under membrane action', J. Struct. Eng., 123 (10), (1997), pp 1331-1338.

[33] Fu, Q.N., Tan, K.H., Zhou, X.H. and Yang, B., 'A mechanical model of composite floor systems under an internal column removal scenario', Engineering Structures 175, (2018), pp 50-62.

Figure captions

Figure 1: Different continuity possibilities for the panel under consideration.

Figure 2: The horizontal force system between facets along the yield lines and at edges, for *x*-aligned mechanisms.

Figure 3: The horizontal force system between facets along the yield lines and at edges, for *y*-aligned mechanisms.

Figure 4: Geometry of diagonal yield-line crack opening. (a) Crack opening at rebar level; (b) Top surface of slab, including rigid-body movements of triangular and trapezoidal slab facets.

Figure 5: Projection on the *x*-direction of the yield lines at different stages; (a) Concrete stress blocks on all yield lines; (b) Triangular stress blocks above rebar on diagonal yield lines; (c) Triangular stress blocks below rebar on diagonal yield lines; (d) Trapezoidal stress blocks on diagonal yield lines.

Figure 6: Forces and neutral axis depths at the edges of a continuous rectangular slab.

Figure 7: Panel edge forces with: (i) rotational continuity and (b) unfractured mesh, (c) fractured mesh; (ii) axial and rotational continuity and (e) unfractured mesh, (f) fractured mesh. Original states are shown as (a) and (d).

Figure 8: Forces involved in equilibrium of moments for triangular facet about the edge axis X'X", and for trapezoidal facet about edge axis Y'Y".

Figure 9: Effect of bar fracture on capacity of rectangular 9.50m x 6.46m slab: (a) a panel with rotational continuity across all edges; (b) a simply supported panel. Mesh effective depth is 30mm.

Figure 10: Effect of bar fracture on capacity of square 6.46m x 6.46m slab: (a) a panel with rotational continuity across all edges; (b) a simply supported panel. Mesh effective depth is 30mm.

Figure 11: Variation of capacity with different edge rotational continuity for isotropically-reinforced slabs of aspect ratio 1.4706 with mesh at 30mm (a, b), 68mm (c, d), 90mm (e, f) depth: (a, c, e) Grade B smooth mesh (fracture crack-width 5.43mm; (b, d, f) Grade C smooth mesh (fracture crack-width 11.08mm.

Figure 12: (a) Comparison of the new method with Wood's [2] Test FS12 on a square slab with heavily restrained edges. (b) Setup for Wood's test FS12.

Figure 13: Events which control the development of compressive and tensile membrane action of the fully restrained slab; (a) with mesh of effectively infinite ductility; (b) with fracture crack-width of 11.08 mm.

Figure 14: Effect of edge restraint conditions on the capacity of a "Garston" slab panel with reference to mesh fracture crack-width: (a) effectively infinite ductility; (b) 11.08 mm; (c) 5.43 mm; (d) 1.01 mm.

Figure 15: Effect of mesh size on the development of tensile membrane action for effectively infinite mesh ductility. Cases with edge restraint are plotted in black; those with no edge restraint are plotted in red. Mesh bar diameter is marked on pairs of curves.

Figure 16: Effect of reinforcement bar ductility (as fracture crack-width) on the development of tensile membrane action for slabs with edge restraint.

Table captions

Table 1: Possible combinations of concrete stress block and rebar fracture in *x*-aligned mechanism.

Table 2: *x*-aligned mechanisms: General form of each equation $a\psi_1^2 + b\psi_1 + c = 0$

Table 3: *x*-aligned mechanisms: General form of each equation $a\psi_1^2 + b\psi_1 + c = 0$

Table 4: *x*-aligned mechanisms: General form of each equation $a\psi_1^2 + b\psi_1 + c = 0$

Table 5: Possible combinations of concrete stress block and rebar fracture in *y*-aligned mechanism.

Table 6: *y*-aligned mechanisms: General form of each equation $a\psi_1^2 + b\psi_1 + c = 0$

Table 7: *y*-aligned mechanisms: General form of each equation $a\psi_1^2 + b\psi_1 + c = 0$

Table 8: *y*-aligned mechanisms: General form of each equation $a\psi_1^2 + b\psi_1 + c = 0$

Table 9: Fracture crack-widths for meshes of ductility classes B and C used in case studies.

Notation List

A_1, A_{2x}, A_{2y}	Area of concrete compression blocks at central and diagonal yield lines.
B_c, C_c	Terms in in-plane equilibrium equations due to restraint to movement at edges of the slab.
C_s	Term in in-plane equilibrium equations due to continuity of reinforcement across edges of the slab.
C_1	Concrete resultant force across a diagonal yield line.
C_{x2}, C_{y2}	Concrete *x*- or *y*- direction resultant forces across central yield line.
C_{x4}, C_{y3}	Boundary resultant in-plane compression forces.
f_{px}, f_{py}	Steel strengths per unit width in *x* and *y* directions.
f_c	Concrete ultimate compressive strength.
f_y, f_u	Steel reinforcement yield and ultimate strengths.
k_{rx}, k_{ry}	Flags (1 or 0) indicating whether rebar in *x*- and *y*-directions is continuous across slab edges.
k_{ax}, k_{ay}	Flags (1 or 0) indicating whether outward movement in *x*- and *y*-directions is restrained at slab edges.
l_d, l'_d	Elastic and plastic bond development lengths.
l_y	*y*-direction slab dimension.
M_{CS}, M'_{CS}	Moments including C_1 and S about *y*-aligned or *x*-aligned edge respectively.
M_{Cx2}, M'_{Cy2}	Moments of C_{x2}, C_{y2} about *y*-aligned or *x*-aligned edge respectively.
M_{ext}, M'_{ext}	Total external moment about *y*-aligned or *x*-aligned edge respectively.
$M_{\text{int}}, M'_{\text{int}}$	Total internal moment about *y*-aligned or *x*-aligned edge respectively.
M_{Tx1}, M_{Tx2}	Moments of T_{x1}, T_{x2} about *y*-aligned edge.
M'_{Ty1}, M'_{Ty2}	Moments of T_{y1}, T_{y2} about *x*-aligned edge.
M_V	Moment of V about appropriate edge (depends on facet considered).
n_x, n_y	Dimensionless coordinates of yield line intersection in *x*- and *y*-aligned mechanisms.
p	Uniformly distributed applied load on slab.
r	Aspect ratio of the slab.
S	Resultant in-plane shear force along a diagonal yield line.
$T_{x1}, T_{x2}, T_{y1}, T_{y2}$	Resultant in-plane tension forces in *x*- or *y*-aligned rebar at internal yield lines.
T_{y3}, T_{x4}	Resultant in-plane tension forces in *x*- or *y*-aligned rebar at slab edges.
t	Slab thickness.
u, v	Movements in *x* and *y* directions of a point on the concrete crack surface at a yield line.

x, y, z	Cartesian coordinate system.
$x_{CA1}, y_{CA1}, z_{CA1}$	Centroid coordinates of compression block on diagonal yield line.
$x_{\lim 1y}$	Limiting x-coordinate of unfractured y-direction reinforcement.
x_{t1}	x-coordinate at which y-direction rebar crosses the neutral axis of the compression block on a diagonal yield line.
$y_{\lim 1x}$	Limiting y-coordinate of unfractured x-direction reinforcement.
y_{t1}	y-coordinate at which x-direction rebar crosses the neutral axis of the compression block on a diagonal yield line.
z_1, z_2	Neutral axis depths of diagonal yield line interface at corner and yield line intersection.
z_3, z_4	Neutral axis depths at edges normal to x and y respectively.
δ_A	Transverse deflection at the slab centre.
Δ_x, Δ_y	Movements of facets at corner of slab at x- and y-directions.
$\Delta_{\lim,x}, \Delta_{\lim,y}$	Limiting crack widths in x- and y-directions at which rebar breaks.
γ	Angle between diagonal yield line and y-axis.
$\psi_1, \psi_2, \psi_3, \psi_4$	Dimensionless neutral axis depths $\psi_1 = \frac{z_1}{l_y}, \psi_2 = \frac{z_2}{l_y}, \psi_3 = \frac{z_3}{l_y}, \psi_4 = \frac{z_4}{l_y}$
η_x, η_y	Dimensionless limiting crack widths $\eta_x = \frac{\Delta_{\lim,x}}{l_y}, \eta_y = \frac{\Delta_{\lim,y}}{l_y}$
θ	Rotation of slab facet about y-aligned edge.
ϕ	Rotation of slab facet about x-aligned edge.
μ	Steel mesh depth as a proportion of slab depth.
λ_x, λ_y	Dimensionless strength ratios $\lambda_x = \frac{f_{px}}{f_c}, \lambda_y = \frac{f_{py}}{f_c}$
τ	Dimensionless slab depth $\tau = \frac{t}{l}$.

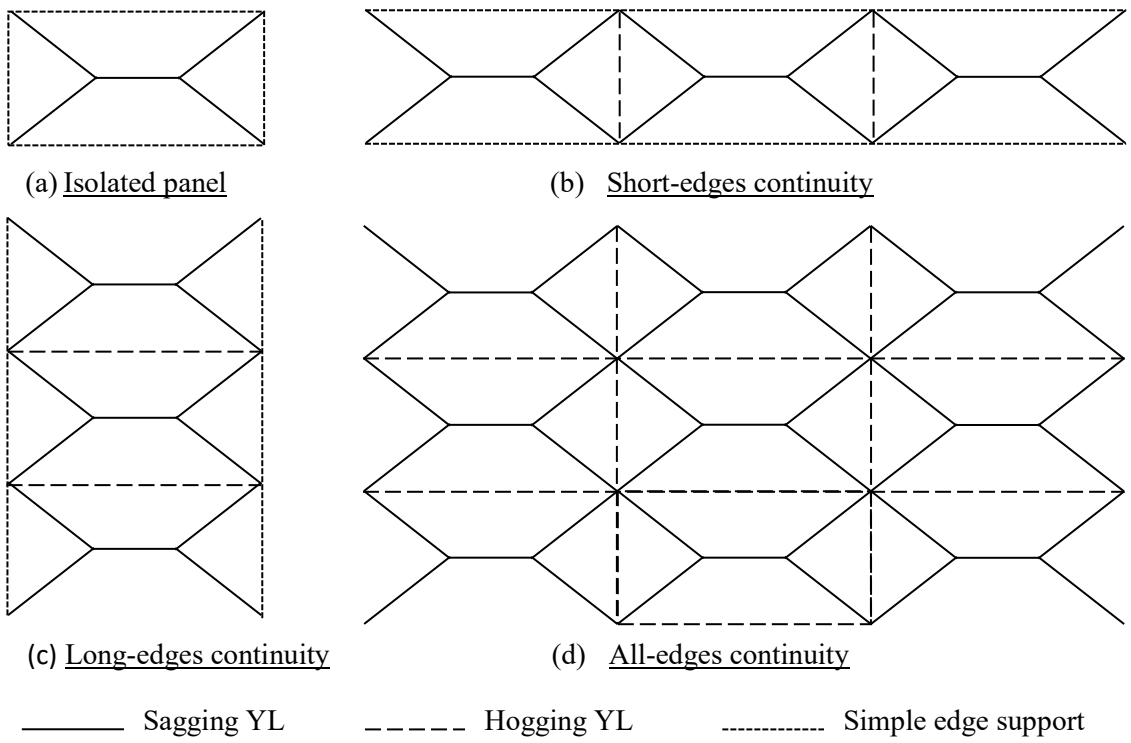

Figure 1: Different continuity possibilities for the panel under consideration.

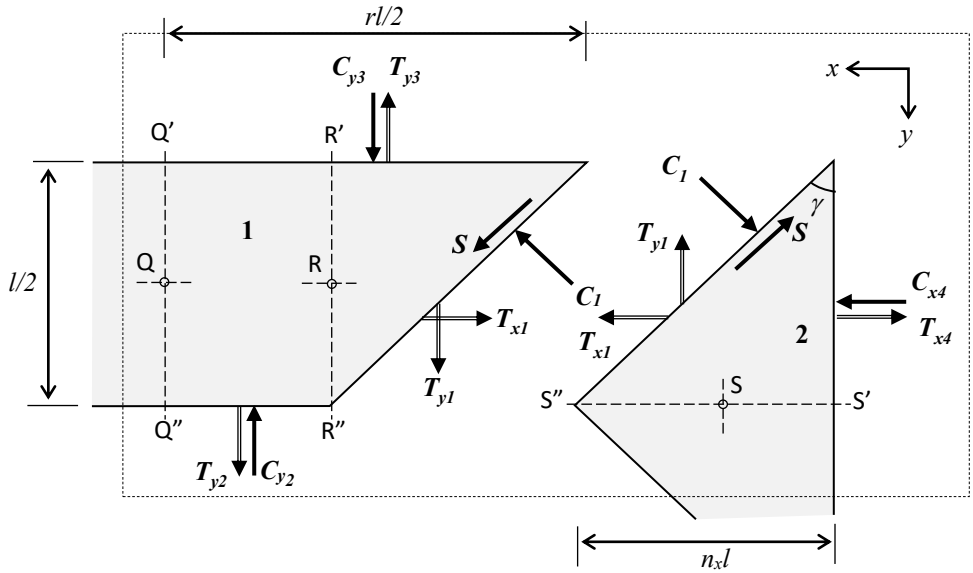

Figure 2: The horizontal force system between facets along the yield lines and at edges, for x-aligned mechanisms.

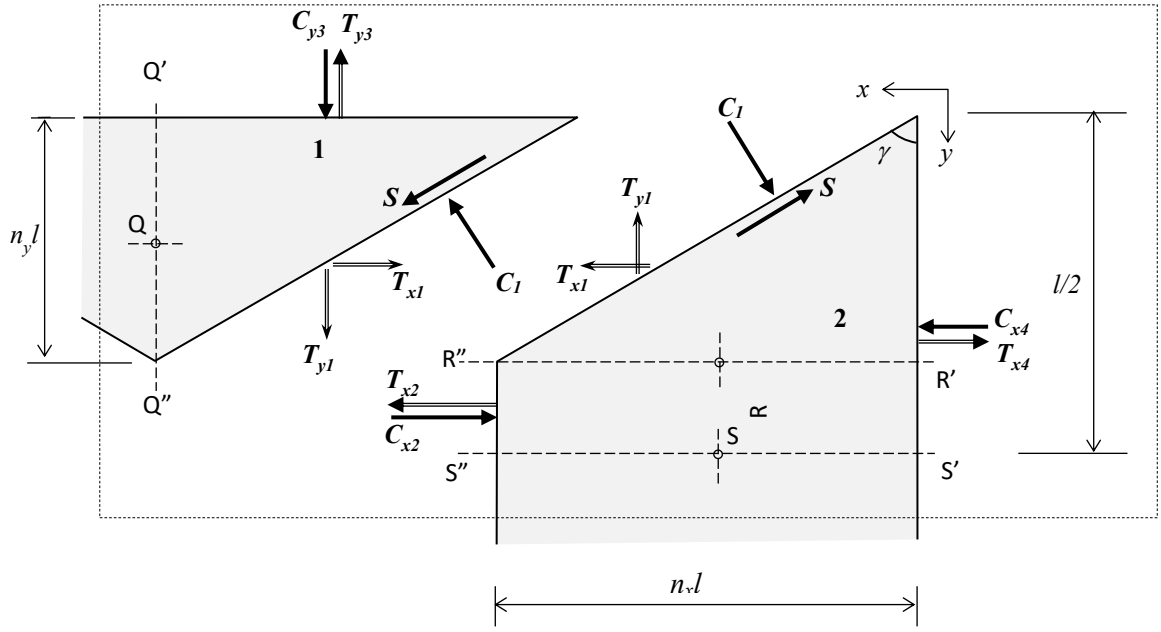

Figure 3: The horizontal force system between facets along the yield lines and at edges, for y-aligned mechanisms.

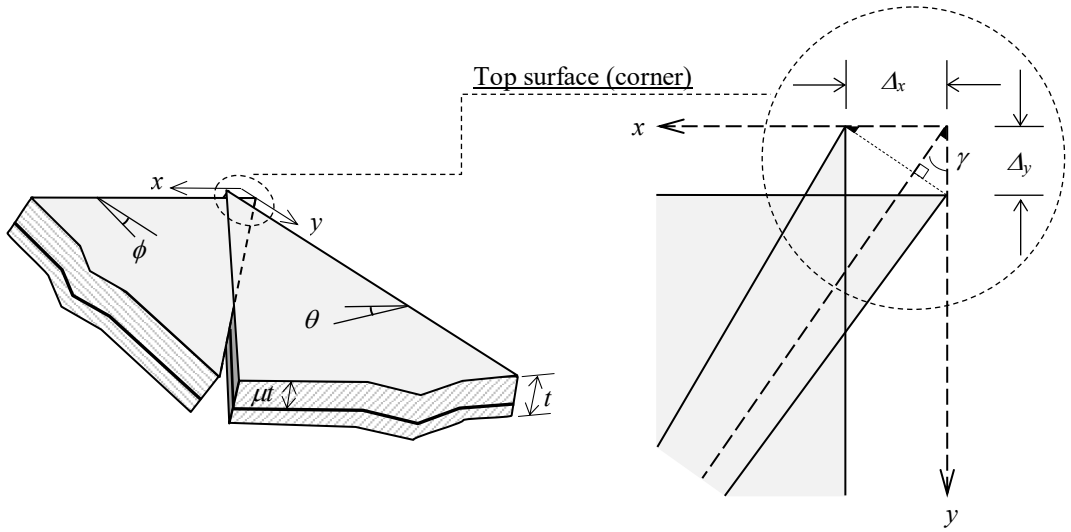

(a) (b) Plan view

Figure 4: Geometry of diagonal yield-line crack opening. (a) Crack opening at rebar level; (b) Top surface of slab, including rigid-body movements of triangular and trapezoidal slab facets.

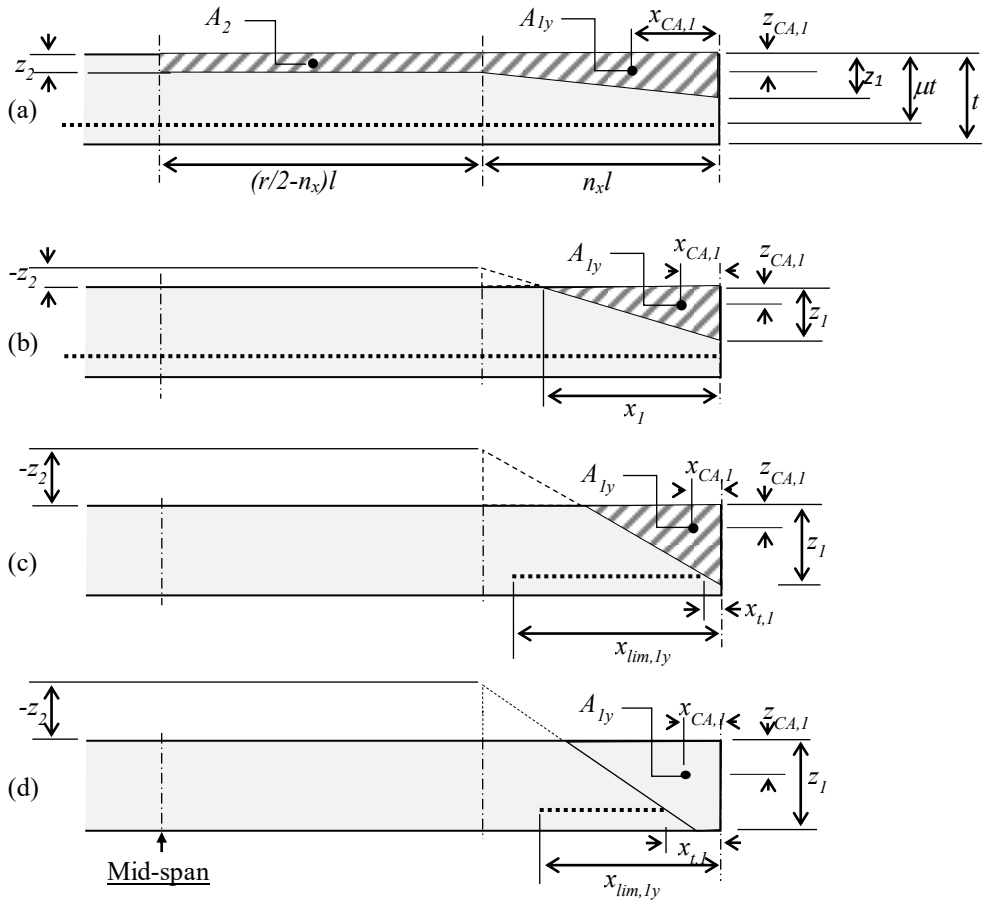

Figure 5: Projection on the x-direction of the yield lines at different stages; (a) Concrete stress blocks on all yield lines; (b) Triangular stress blocks above rebar on diagonal yield lines; (c) Triangular stress blocks below rebar on diagonal yield lines; (d) Trapezoidal stress blocks on diagonal yield lines.

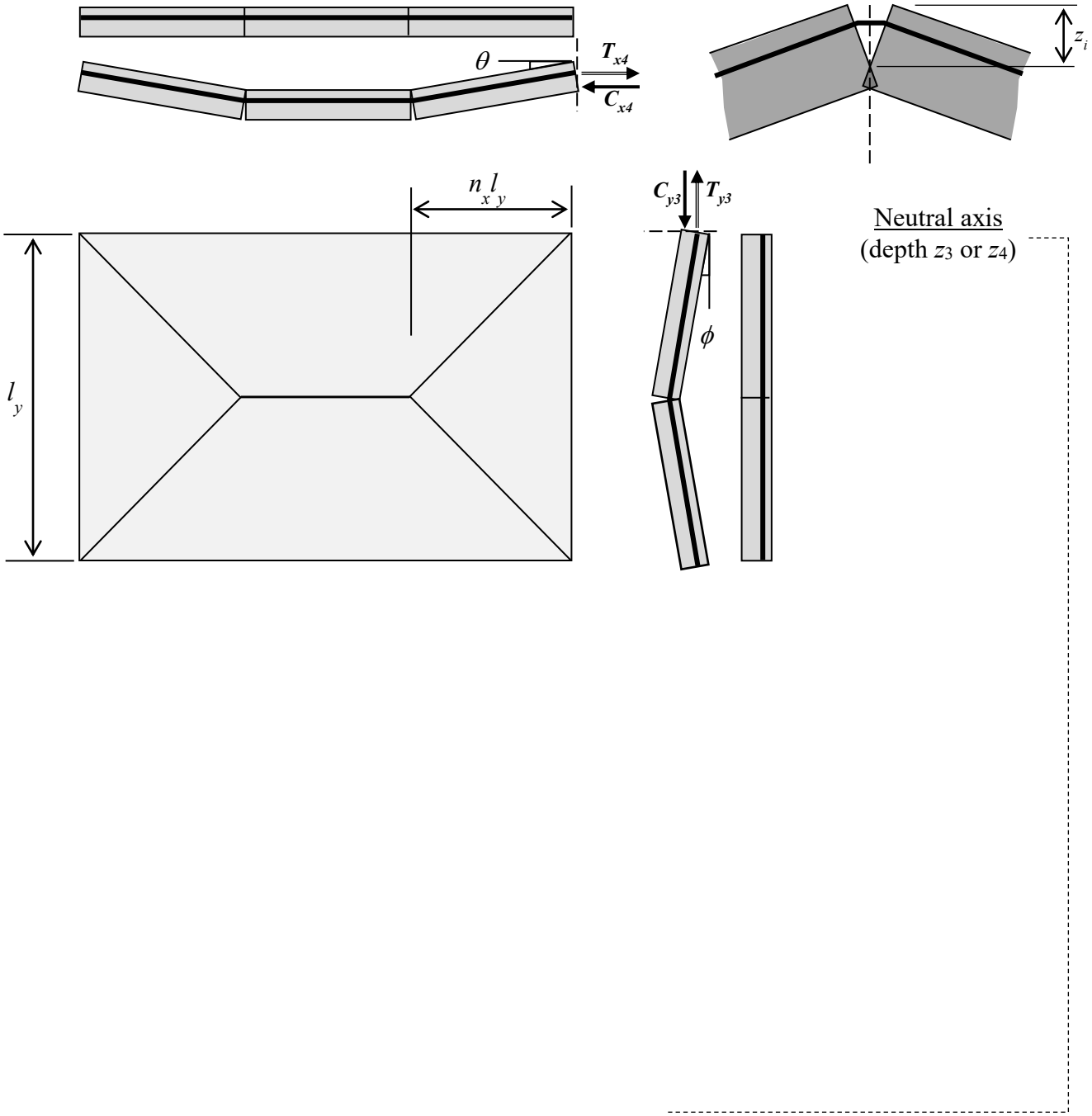

Figure 6: Forces and neutral axis depths at the edges of a continuous rectangular slab.

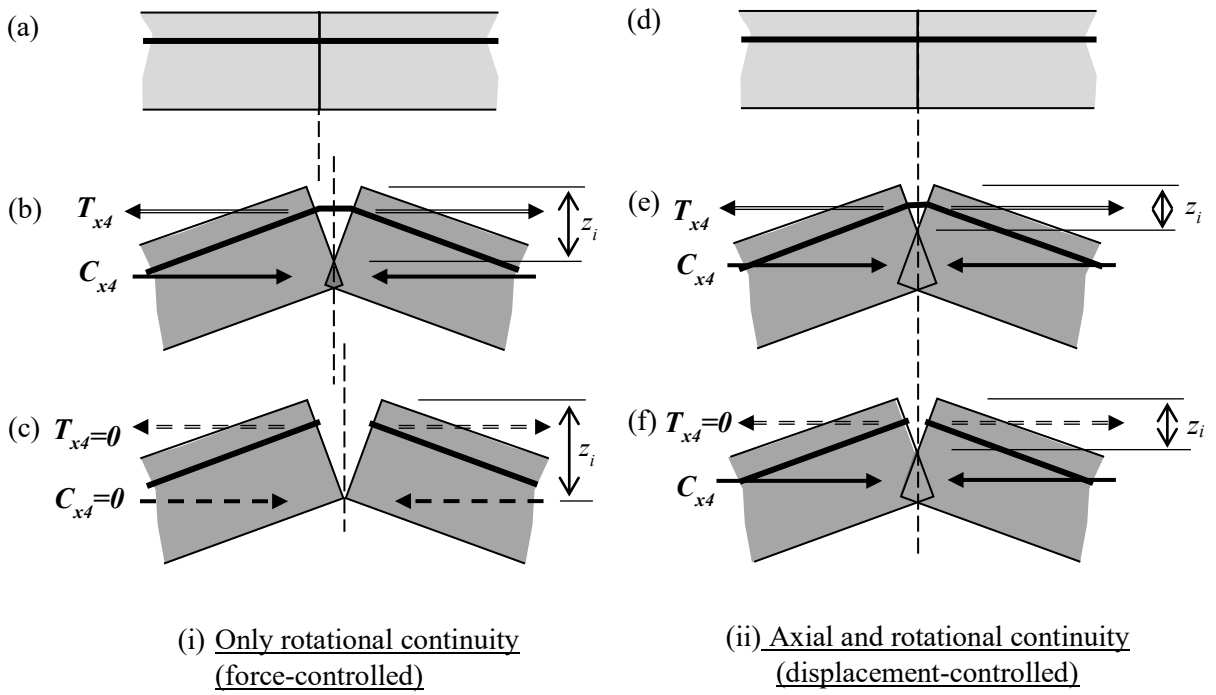

Figure 7: Panel edge forces with: (i) rotational continuity and (b) unfractured mesh, (c) fractured mesh; (ii) axial and rotational continuity and (e) unfractured mesh, (f) fractured mesh. Original states are shown as (a) and (d).

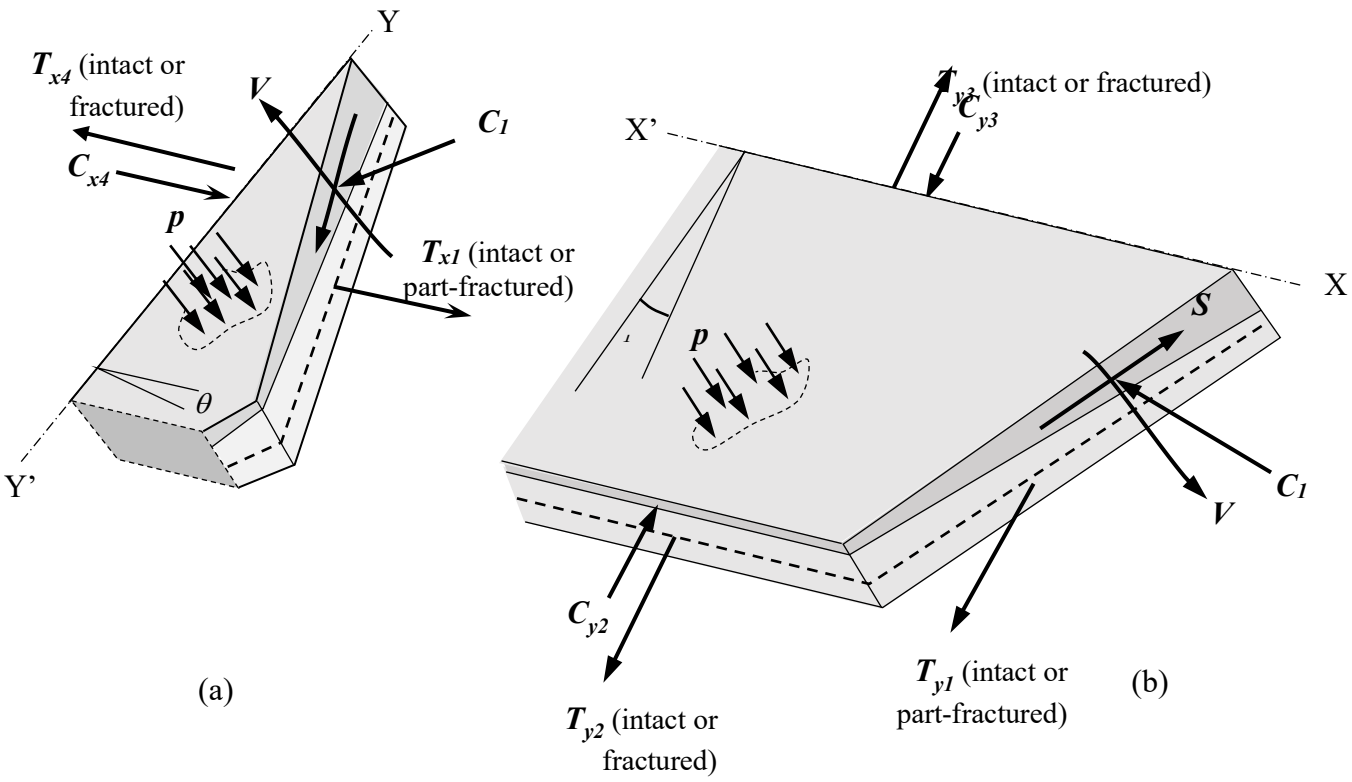

Figure 8: Forces involved in equilibrium of moments for triangular facet about the edge axis X'X", and for trapezoidal facet about edge axis Y'Y".

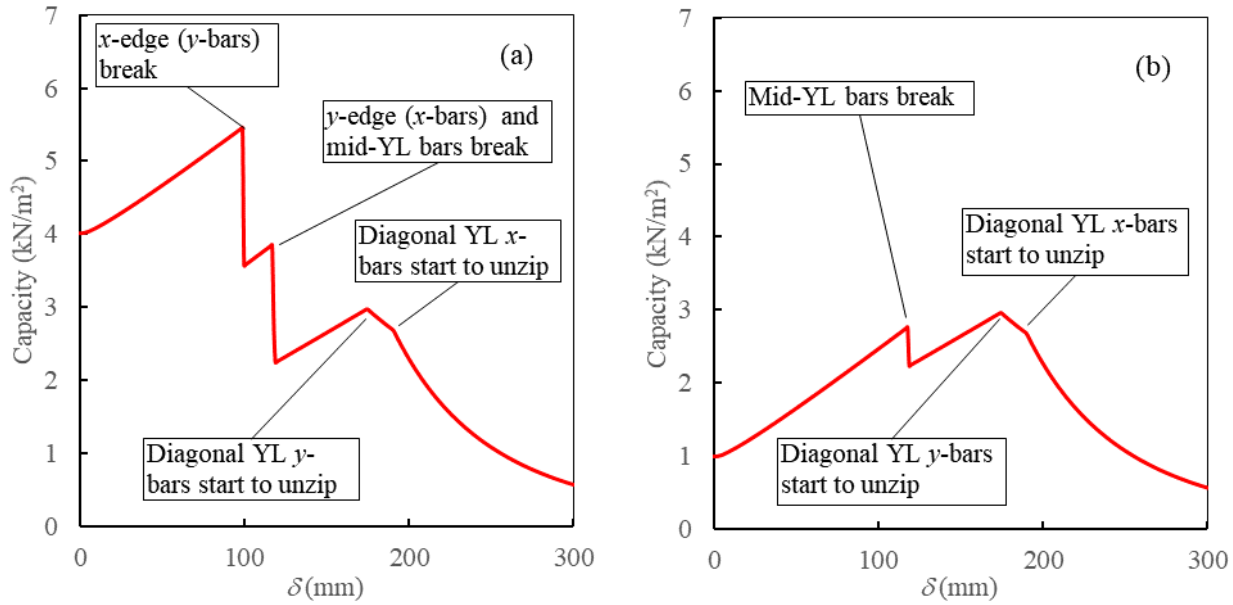

Figure 9: Effect of bar fracture on capacity of rectangular 9.50m x 6.46m slab: (a) a panel with rotational continuity across all edges; (b) a simply supported panel. Mesh effective depth is 30mm.

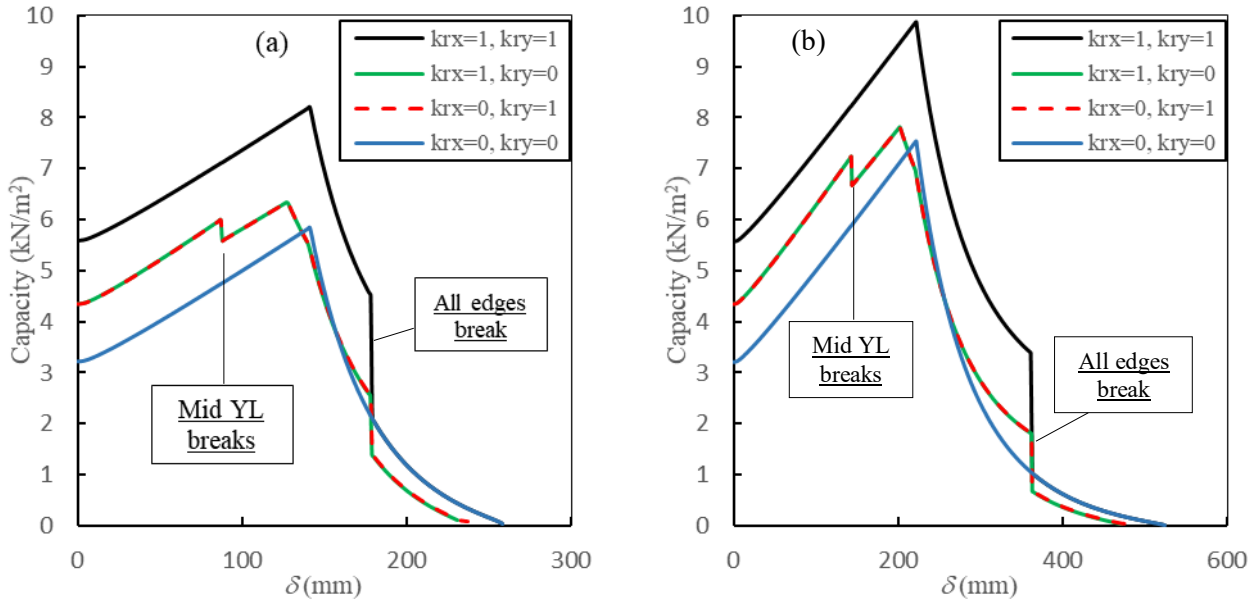

Figure 10: Effect of bar fracture on capacity of square 6.46m x 6.46m slab: (a) a panel with rotational continuity across all edges; (b) a simply supported panel. Mesh effective depth is 30mm.

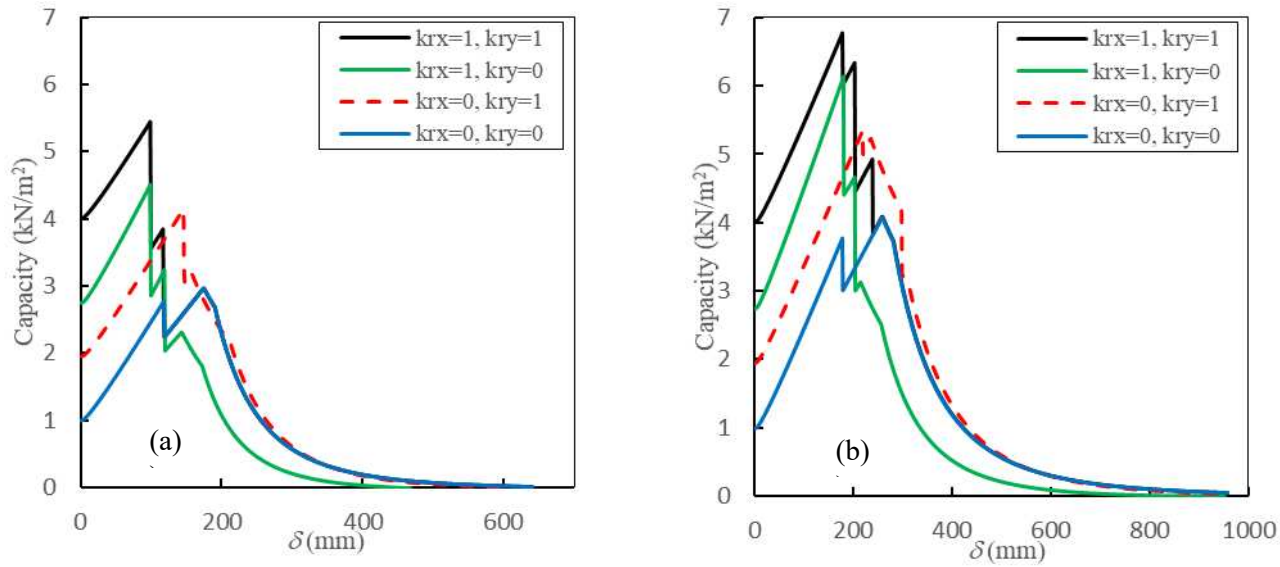

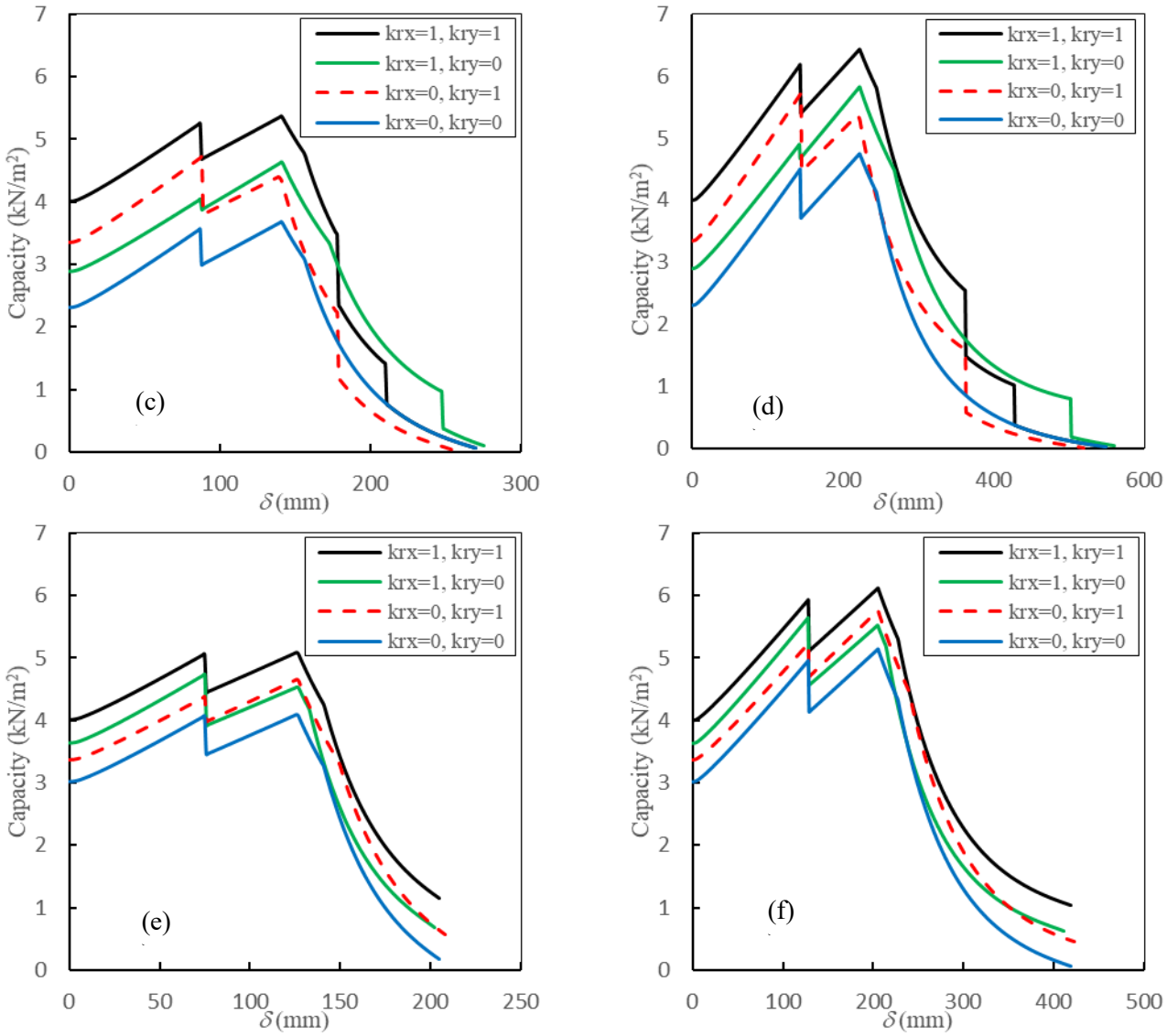

Figure 11: Variation of capacity with different edge rotational continuity for isotropically-reinforced slabs of aspect ratio 1.4706 with mesh at 30mm (a, b), 68mm (c, d), 90mm (e, f) depth: (a, c, e) Grade B smooth mesh (fracture crack-width 5.45mm; (b, d, f) Grade C smooth mesh (fracture crack-width 11.08mm.

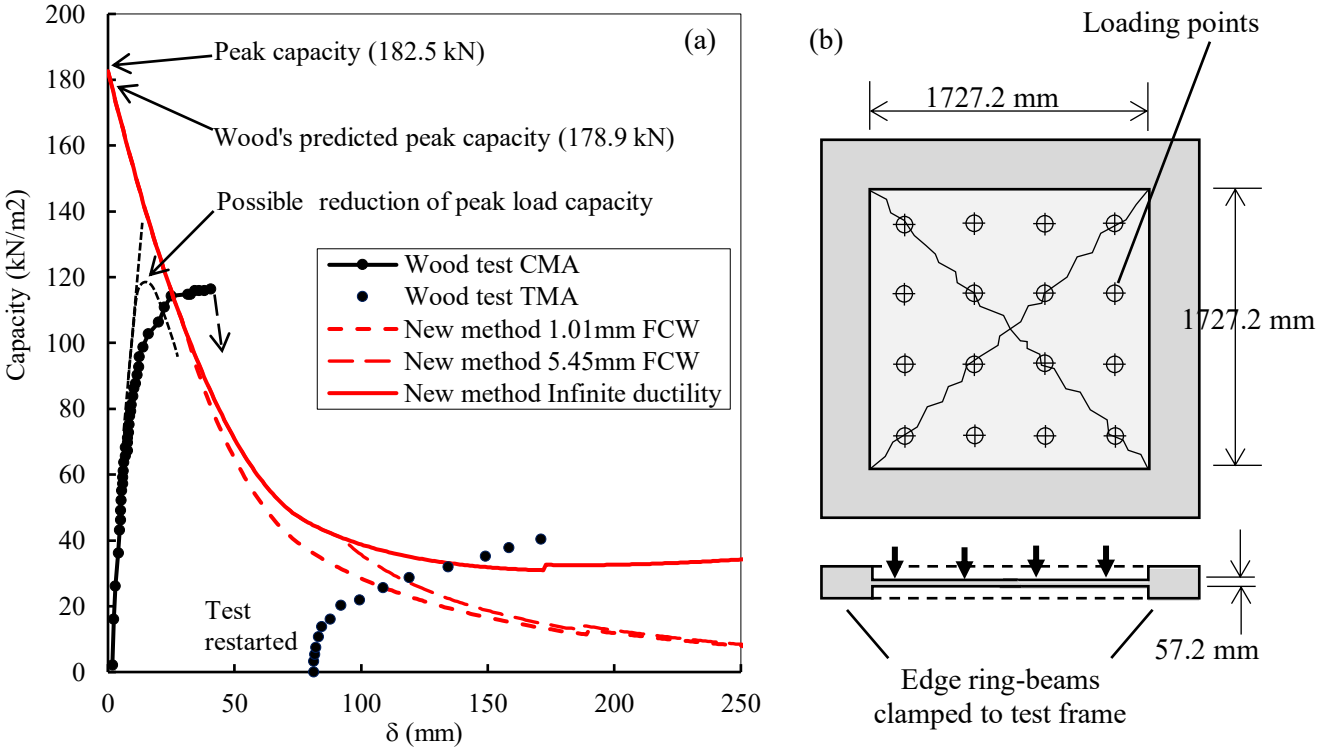

Figure 12 (a) Comparison of the new method with Wood's [2] Test FS12 on a square slab with heavily restrained edges. (b) Setup for Wood's test FS12.

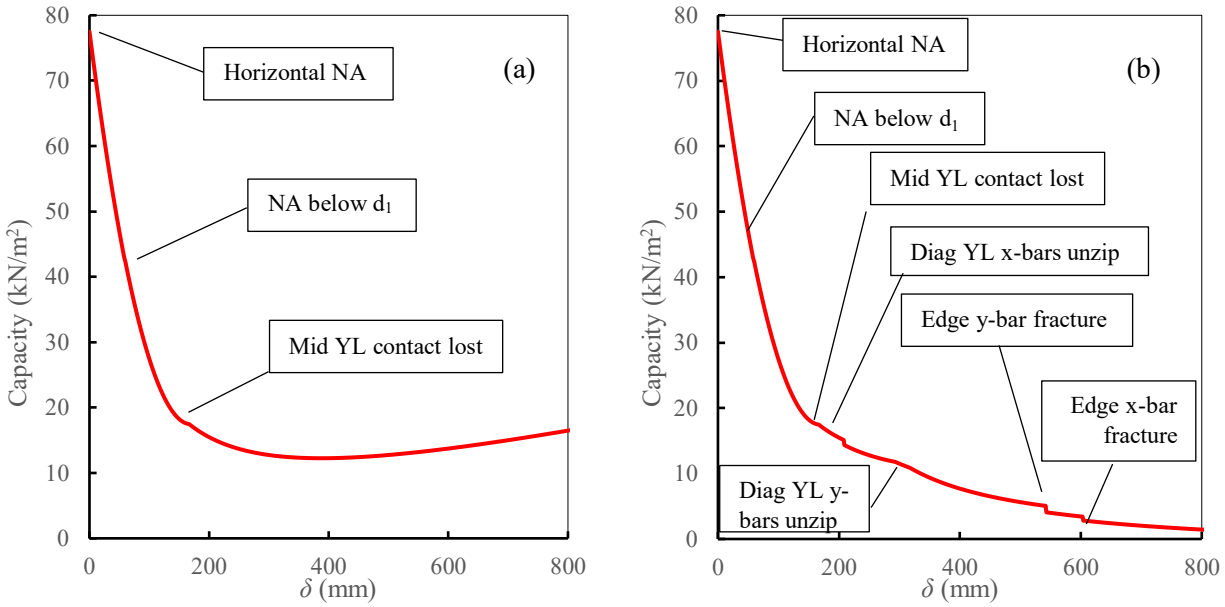

Figure 13: Events which control the development of compressive and tensile membrane action of the fully restrained slab; (a) with mesh of effectively infinite ductility; (b) with fracture crack-width of 11.08 mm.

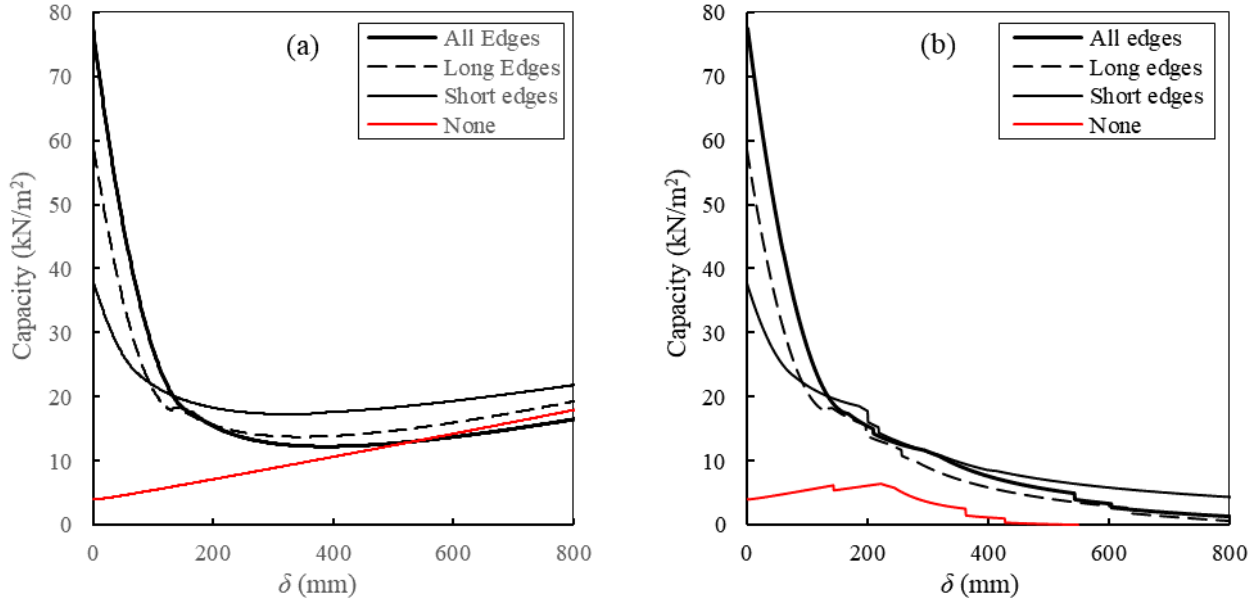

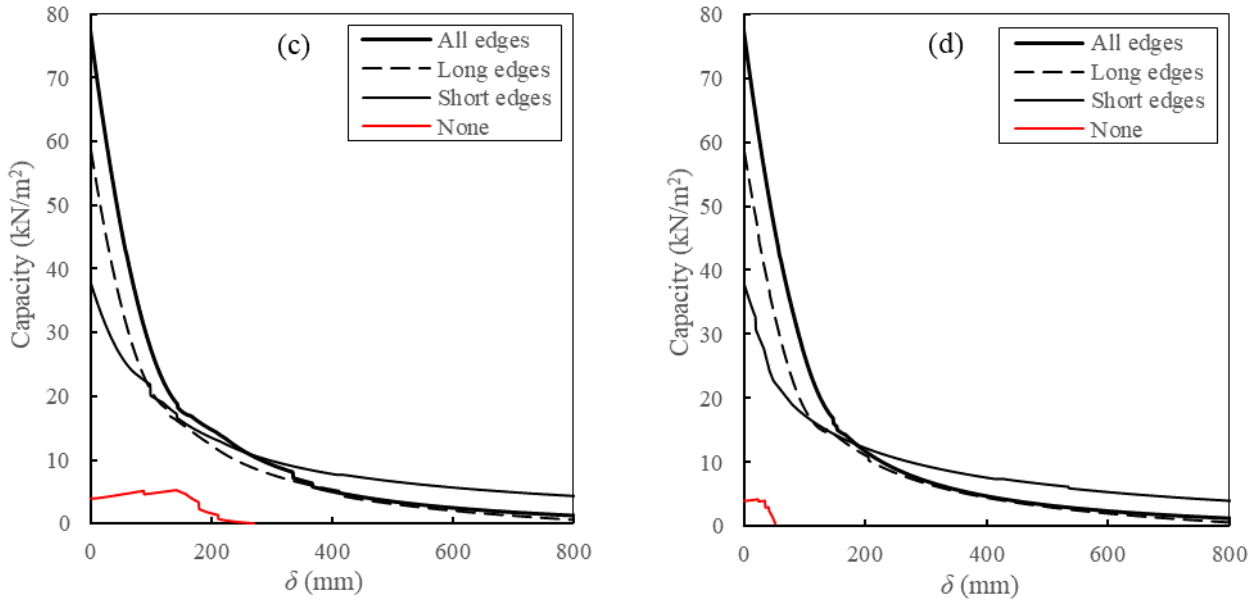

Figure 14: Effect of edge restraint conditions on the capacity of a "Garston" slab panel with reference to mesh fracture crack-width: (a) effectively infinite ductility; (b) 11.08 mm; (c) 5.43 mm; (d) 1.01 mm.

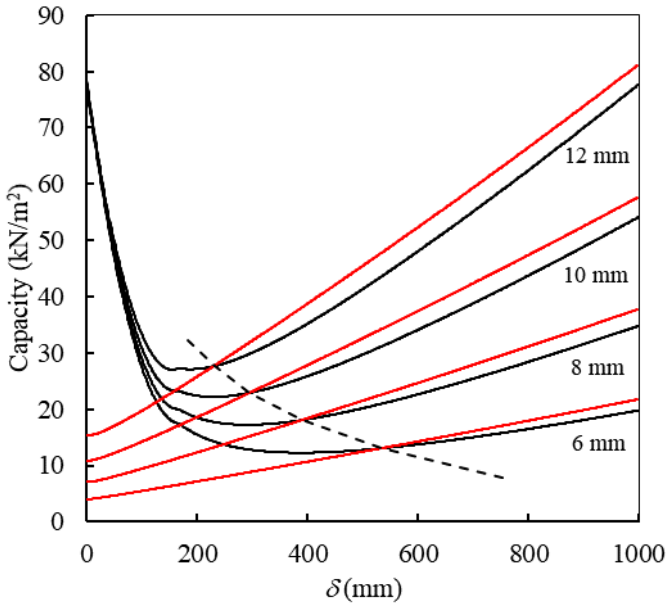

Figure 15: Effect of mesh size on the development of tensile membrane action for effectively infinite mesh ductility. Cases with edge restraint are plotted in black; those with no edge restraint are plotted in red. Mesh bar diameter is marked on pairs of curves.

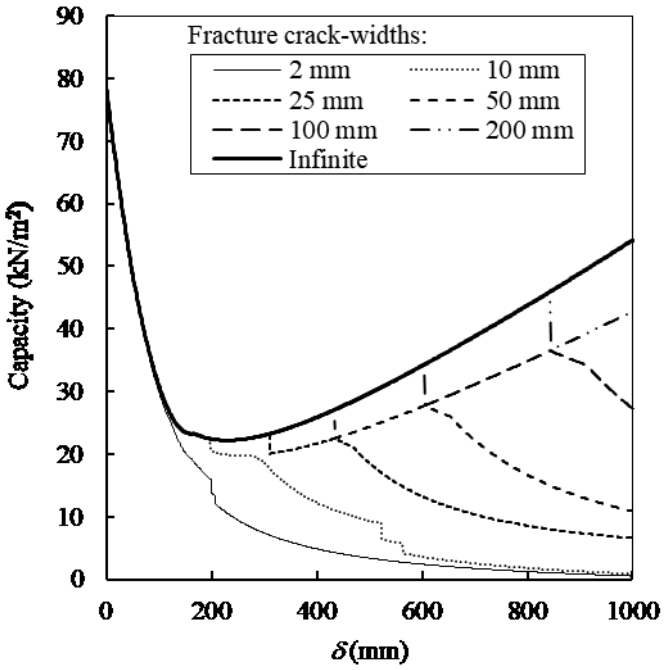

Figure 16: Effect of reinforcement bar ductility (as fracture crack-width) on the development of tensile membrane action for slabs with edge restraint..

Table 1: Possible combinations of concrete stress block and rebar fracture in x-aligned mechanism.

Compression block		Rebar mesh fracture condition					
		None	Central *y*	Diagonal *x*	Central *y* + diagonal *x*	Central *y* + diagonal *y*	diagonal *x* and *y*
Full	Above mesh ($z1<\mu t, z2>0$)	*a1x*	*a1x'*	*a1x**	*a1x'**	*a1x***	*a1x****
	Below mesh ($z1>\mu t, z2>0$)	*a2x*	*a2x'*	*a2x**	*a2x'**	*a2x***	*a2x****
Triangular	Above mesh ($z1<\mu t, z2<0$)	*b1x*	*b1x'*	*b1x**	*b1x'**	*b1x***	*b1x****
	Below mesh ($z1>\mu t, z2<0$)	*b2x*	*b2x'*	*b2x**	*b2x'**	*b2x***	*b2x****
Trapezoidal	($z1>t, z2<0$)	*cx*	*cx'*	*cx**	*cx'**	*cx***	*cx****

Table 2: x-aligned mechanisms: General form of each equation $a\psi_1^2 + b\psi_1 + c = 0$

Case	*a*	*b*		*c*	
a1x		$n_x\left(\frac{1}{\sin\gamma\cos\gamma}+r-2n_x\right)+B_c$		$-\frac{n_x^2\theta}{2}\left(\frac{1}{2\sin\gamma\cos\gamma}+r-2n_x\right)+C_c$	$-\frac{\lambda_x}{2}-\lambda_y r n_x+C_s$
a1x'		$n_x\left(\frac{1}{\sin\gamma\cos\gamma}+r-2n_x\right)+B_c$		$-\frac{n_x^2\theta}{2}\left(\frac{1}{2\sin\gamma\cos\gamma}+r-2n_x\right)+C_c$	$-\frac{\lambda_x}{2}-2\lambda_y n_x^2+C_s$
*a1x**		$n_x\left(\frac{1}{\sin\gamma\cos\gamma}+r-2n_x\right)+B_c$	$-\frac{\lambda_x}{\theta n_x}$	$-\frac{n_x^2\theta}{2}\left(\frac{1}{2\sin\gamma\cos\gamma}+r-2n_x\right)+C_c$	$-\frac{\lambda_x}{\theta^2 n_x}(\eta_x-\theta\mu\tau)-\lambda_y r n_x+C_s$
*a1x'**		$n_x\left(\frac{1}{\sin\gamma\cos\gamma}+r-2n_x\right)+B_c$	$-\frac{\lambda_x}{\theta n_x}$	$-\frac{n_x^2\theta}{2}\left(\frac{1}{2\sin\gamma\cos\gamma}+r-2n_x\right)+C_c$	$-\frac{\lambda_x}{\theta^2 n_x}(\eta_x-\theta\mu\tau)-2\lambda_y n_x^2+C_s$
*a1x***		$n_x\left(\frac{1}{\sin\gamma\cos\gamma}+r-2n_x\right)+B_c$	$-\frac{4n_x\lambda_y}{\theta}$	$-\frac{n_x^2\theta}{2}\left(\frac{1}{2\sin\gamma\cos\gamma}+r-2n_x\right)+C_c$	$-\frac{\lambda_x}{2}-\frac{2\lambda_y}{\theta^2}(\eta_y-2n_x\theta\mu\tau)+C_s$
*a1x****		$n_x\left(\frac{1}{\sin\gamma\cos\gamma}+r-2n_x\right)+B_c$	$-\frac{\lambda_x}{\theta n_x}-\frac{4n_x\lambda_y}{\theta}$	$-\frac{n_x^2\theta}{2}\left(\frac{1}{2\sin\gamma\cos\gamma}+r-2n_x\right)+C_c$	$-\frac{\lambda_x}{\theta^2 n_x}(\eta_x-\theta\mu\tau)-\frac{2\lambda_y}{\theta^2}(\eta_y-2n_x\theta\mu\tau)+C_s$
a2x		$n_x\left(\frac{1}{\sin\gamma\cos\gamma}+r-2n_x\right)+B_c$	$+\frac{\lambda_x}{\theta n_x}+\frac{4n_x\lambda_y}{\theta}$	$-\frac{n_x^2\theta}{2}\left(\frac{1}{2\sin\gamma\cos\gamma}+r-2n_x\right)+C_c$	$-\lambda_x(\frac{1}{2}+\frac{\mu\tau}{\theta n_x})-\lambda_y n_x(r+\frac{4\mu\tau}{\theta})+C_s$
a2x'		$n_x\left(\frac{1}{\sin\gamma\cos\gamma}+r-2n_x\right)+B_c$	$+\frac{\lambda_x}{\theta n_x}+\frac{4n_x\lambda_y}{\theta}$	$-\frac{n_x^2\theta}{2}\left(\frac{1}{2\sin\gamma\cos\gamma}+r-2n_x\right)+C_c$	$-\lambda_x(\frac{1}{2}+\frac{\mu\tau}{\theta n_x})-\lambda_y n_x(2n_x+\frac{4\mu\tau}{\theta})+C_s$
*a2x**		$n_x\left(\frac{1}{\sin\gamma\cos\gamma}+r-2n_x\right)+B_c$	$+\frac{4n_x\lambda_y}{\theta}$	$-\frac{n_x^2\theta}{2}\left(\frac{1}{2\sin\gamma\cos\gamma}+r-2n_x\right)+C_c$	$-\frac{\lambda_x\eta_x}{\theta^2 n_x}-\lambda_y n_x(r+\frac{4\mu\tau}{\theta})+C_s$
*a2x'**		$n_x\left(\frac{1}{\sin\gamma\cos\gamma}+r-2n_x\right)+B_c$	$+\frac{4n_x\lambda_y}{\theta}$	$-\frac{n_x^2\theta}{2}\left(\frac{1}{2\sin\gamma\cos\gamma}+r-2n_x\right)+C_c$	$-\frac{\lambda_x\eta_x}{\theta^2 n_x}-\lambda_y n_x(2n_x+\frac{4\mu\tau}{\theta})+C_s$
*a2x***		$n_x\left(\frac{1}{\sin\gamma\cos\gamma}+r-2n_x\right)+B_c$	$+\frac{\lambda_x}{\theta n_x}$	$-\frac{n_x^2\theta}{2}\left(\frac{1}{2\sin\gamma\cos\gamma}+r-2n_x\right)+C_c$	$-\lambda_x(\frac{1}{2}+\frac{\mu\tau}{\theta n_x})-\frac{2\lambda_y\eta_y}{\theta^2}+C_s$
*a2x****		$n_x\left(\frac{1}{\sin\gamma\cos\gamma}+r-2n_x\right)+B_c$		$-\frac{n_x^2\theta}{2}\left(\frac{1}{2\sin\gamma\cos\gamma}+r-2n_x\right)+C_c$	$-\frac{\lambda_x\eta_x}{\theta^2 n_x}-\frac{2\lambda_y\eta_y}{\theta^2}+C_s$

The continuity terms are $B_c=\frac{k_{cx}}{2}+k_{cy}rn_x$, $C_c=-\frac{k_{cx}\tau}{2}-k_{cy}\tau rn_x$, $C_s=\frac{k_{cx}k_{rx}\lambda_x}{2}+k_{cy}k_{ry}rn_x\lambda_y$.

Table 3: x-aligned mechanisms: General form of each equation $a\psi_1^2 + b\psi_1 + c = 0$

Case	*a*	*b*	*c*
b1x	$\frac{1}{\theta \sin\gamma \cos\gamma}$	B_c	$-\frac{\lambda_x}{2} - \lambda_y r n_x + C_c + C_s$
b1x'	$\frac{1}{\theta \sin\gamma \cos\gamma}$	B_c	$-\frac{\lambda_x}{2} - 2\lambda_y n_x^2 + C_c + C_s$
*b1x**	$\frac{1}{\theta \sin\gamma \cos\gamma}$	$-\frac{\lambda_x}{\theta n_x} + B_c$	$-\frac{\lambda_x}{\theta n_x}(\frac{\eta_x}{\theta} - \mu\tau) - \lambda_y r n_x + C_c + C_s$
*b1x'**	$\frac{1}{\theta \sin\gamma \cos\gamma}$	$-\frac{\lambda_x}{\theta n_x} + B_c$	$-\frac{\lambda_x}{\theta n_x}(\frac{\eta_x}{\theta} - \mu\tau) - 2\lambda_y n_x^2 + C_c + C_s$
*b1x***	$\frac{1}{\theta \sin\gamma \cos\gamma}$	$-\frac{4\lambda_y n_x}{\theta} + B_c$	$-\frac{\lambda_x}{2} - \frac{\lambda_y}{\theta}(\frac{2\eta_y}{\theta} - 4n_x\mu\tau) + C_c + C_s$
*b1x****	$\frac{1}{\theta \sin\gamma \cos\gamma}$	$-\frac{\lambda_x}{\theta n_x} - \frac{4\lambda_y n_x}{\theta} + B_c$	$-\frac{\lambda_x}{\theta n_x}(\frac{\eta_x}{\theta} - \mu\tau) - \frac{\lambda_y}{\theta}(\frac{2\eta_y}{\theta} - 4n_x\mu\tau) + C_c + C_s$
b2x	$\frac{1}{\theta \sin\gamma \cos\gamma}$	$+\frac{\lambda_x}{\theta n_x} + \frac{4\lambda_y n_x}{\theta} + B_c$	$-\lambda_x(\frac{1}{2} + \frac{\mu\tau}{\theta n_x}) - \lambda_y n_x(r + \frac{4\mu\tau}{\theta}) + C_c + C_s$
b2x'	$\frac{1}{\theta \sin\gamma \cos\gamma}$	$+\frac{\lambda_x}{\theta n_x} + \frac{4\lambda_y n_x}{\theta} + B_c$	$-\lambda_x(\frac{1}{2} + \frac{\mu\tau}{\theta n_x}) - \lambda_y n_x(2n_x + \frac{4\mu\tau}{\theta}) + C_c + C_s$
*b2x**	$\frac{1}{\theta \sin\gamma \cos\gamma}$	$+\frac{4\lambda_y n_x}{\theta} + B_c$	$-\lambda_x \frac{\eta_x}{n_x\theta^2} - \lambda_y n_x(r + \frac{4\mu\tau}{\theta}) + C_c + C_s$
*b2x'**	$\frac{1}{\theta \sin\gamma \cos\gamma}$	$+\frac{4\lambda_y n_x}{\theta} + B_c$	$-\lambda_x \frac{\eta_x}{n_x\theta^2} - \lambda_y n_x(2n_x + \frac{4\mu\tau}{\theta}) + C_c + C_s$
*b2x***	$\frac{1}{\theta \sin\gamma \cos\gamma}$	$+\frac{\lambda_x}{\theta n_x} + B_c$	$-\lambda_x(\frac{1}{2} + \frac{\mu\tau}{\theta n_x}) - \frac{2\lambda_y \eta_y}{\theta^2} + C_c + C_s$
*b2x****	$\frac{1}{\theta \sin\gamma \cos\gamma}$		$-\frac{\lambda_x \eta_x}{\theta^2 n_x} - \frac{2\lambda_y \eta_y}{\theta^2} + C_c + C_s$

The continuity terms are $B_c = \frac{k_{cx}}{2} + k_{cy} r n_x$, $C_c = -\frac{k_{cx}\tau}{2} - k_{cy}\tau r n_x$, $C_s = \frac{k_{cx}k_{rx}\lambda_x}{2} + k_{cy}k_{ry} r n_x \lambda_y$.

Table 4: x-aligned mechanisms: General form of each equation $a\psi_1^2 + b\psi_1 + c = 0$

Case	*a*	*b*		*c*	
cx		$\frac{2\tau}{\theta\sin\gamma\cos\gamma} + B_c$	$+\frac{\lambda_x}{\theta n_x} + \frac{4\lambda_y n_x}{\theta}$	$-\frac{\tau^2}{\theta\sin\gamma\cos\gamma} + C_c$	$-\lambda_x(\frac{1}{2} + \frac{\mu\tau}{\theta n_x}) - \lambda_y(rn_x + \frac{4\mu\tau n_x}{\theta}) + C_s$
cx'		$\frac{2\tau}{\theta\sin\gamma\cos\gamma} + B_c$	$+\frac{\lambda_x}{\theta n_x} + \frac{4\lambda_y n_x}{\theta}$	$-\frac{\tau^2}{\theta\sin\gamma\cos\gamma} + C_c$	$-\lambda_x(\frac{1}{2} + \frac{\mu\tau}{\theta n_x}) - \lambda_y(2n_x^2 + \frac{4\mu\tau n_x}{\theta}) + C_s$
*cx**		$\frac{2\tau}{\theta\sin\gamma\cos\gamma} + B_c$	$+\frac{4\lambda_y n_x}{\theta}$	$-\frac{\tau^2}{\theta\sin\gamma\cos\gamma} + C_c$	$-\frac{\lambda_x\eta_x}{\theta^2 n_x} - \lambda_y(rn_x + \frac{4\mu\tau n_x}{\theta}) + C_s$
*cx'**		$\frac{2\tau}{\theta\sin\gamma\cos\gamma} + B_c$	$+\frac{4\lambda_y n_x}{\theta}$	$-\frac{\tau^2}{\theta\sin\gamma\cos\gamma} + C_c$	$-\frac{\lambda_x\eta_x}{\theta^2 n_x} - \lambda_y(2n_x^2 + \frac{4\mu\tau n_x}{\theta}) + C_s$
*cx***		$\frac{2\tau}{\theta\sin\gamma\cos\gamma} + B_c$	$+\frac{\lambda_x}{n_x\theta}$	$-\frac{\tau^2}{\theta\sin\gamma\cos\gamma} + C_c$	$-\lambda_x(\frac{1}{2} + \frac{\mu\tau}{\theta n_x}) - \frac{2\lambda_y\eta_y}{\theta^2} + C_s$
*cx****		$\frac{2\tau}{\theta\sin\gamma\cos\gamma} + B_c$		$-\frac{\tau^2}{\theta\sin\gamma\cos\gamma} + C_c$	$-\frac{\lambda_x\eta_x}{\theta^2 n_x} - \frac{2\lambda_y\eta_y}{\theta^2} + C_s$

The continuity terms are $B_c = \frac{k_{cx}}{2} + k_{cy} r n_x$, $C_c = -\frac{k_{cx}\tau}{2} - k_{cy}\tau r n_x$, $C_s = \frac{k_{cx}k_{rx}\lambda_x}{2} + k_{cy}k_{ry}rn_x\lambda_y$.

Table 5: Possible combinations of concrete stress block and rebar fracture in y-aligned mechanism.

Compression block		Rebar mesh fracture condition					
		None	Central *x*	Diagonal *y*	Central *x* + diagonal *y*	Central *x* + diagonal *x*	Diagonal *x* and *y*
Full	Above mesh ($z1<\mu t$, $z2>0$)	*a1y*	*a1y'*	*a1y**	*a1y'**	*a1y***	*a1y****
	Below mesh ($z1>\mu t$, $z2>0$)	*a2y*	*a2y'*	*a2y**	*a2y'**	*a2y***	*a2y****
Triangular	Above mesh ($z1<\mu t$, $z2<0$)	*b1y*	*b1y'*	*b1y**	*b1y'**	*b1y***	*b1y****
	Below mesh ($z1>\mu t$, $z2<0$)	*b2y*	*b2y'*	*b2y**	*b2y'**	*b2y***	*b2y****
Trapezoidal	($z1>t$, $z2<0$)	*cy*	*cy'*	*cy**	*cy'**	*cy***	*cy****

Table 6: y-aligned mechanisms: General form of each equation $a\psi_1^2 + b\psi_1 + c = 0$

	a	b		c	
a1y		$\frac{r}{\sin\gamma\cos\gamma} + 1 - 2n_y + B_c$		$-\frac{\theta r}{4}\left(\frac{r}{2\sin\gamma\cos\gamma} + 1 - 2n_y\right) + C_c$	$-\lambda_x - \frac{\lambda_y r^2}{2n_y} + C_s$
a1y'		$\frac{r}{\sin\gamma\cos\gamma} + 1 - 2n_y + B_c$		$-\frac{\theta r}{4}\left(\frac{r}{2\sin\gamma\cos\gamma} + 1 - 2n_y\right) + C_c$	$-2\lambda_x n_y - \frac{\lambda_y r^2}{2n_y} + C_s$
*a1y**		$\frac{r}{\sin\gamma\cos\gamma} + 1 - 2n_y + B_c$	$-\frac{2\lambda_y r}{\theta n_y}$	$-\frac{\theta r}{4}\left(\frac{r}{2\sin\gamma\cos\gamma} + 1 - 2n_y\right) + C_c$	$-\lambda_x - \frac{2\lambda_y}{\theta^2 n_y}(2\eta_y n_y - \mu\tau r\theta) + C_s$
*a1y'**		$\frac{r}{\sin\gamma\cos\gamma} + 1 - 2n_y + B_c$	$-\frac{2\lambda_y r}{\theta n_y}$	$-\frac{\theta r}{4}\left(\frac{r}{2\sin\gamma\cos\gamma} + 1 - 2n_y\right) + C_c$	$-2\lambda_x n_y - \frac{2\lambda_y}{\theta^2 n_y}(2\eta_y n_y - \mu\tau r\theta) + C_s$
*a1y***		$\frac{r}{\sin\gamma\cos\gamma} + 1 - 2n_y + B_c$	$-\frac{2\lambda_x r}{\theta n_y}$	$-\frac{\theta r}{4}\left(\frac{r}{2\sin\gamma\cos\gamma} + 1 - 2n_y\right) + C_c$	$-\frac{2\lambda_x r}{\theta^2 n_y}(\eta_x - \mu\tau\theta) - \frac{\lambda_y r^2}{2n_y} + C_s$
*a1y****		$\frac{r}{\sin\gamma\cos\gamma} + 1 - 2n_y + B_c$	$-\frac{2\lambda_x r}{\theta n_y} - \frac{2\lambda_y r}{\theta n_y}$	$-\frac{\theta r}{4}\left(\frac{r}{2\sin\gamma\cos\gamma} + 1 - 2n_y\right) + C_c$	$-\frac{2\lambda_x r}{\theta^2 n_y}(\eta_x - \mu\tau\theta) - \frac{2\lambda_y}{\theta^2 n_y}(2\eta_y n_y - \mu\tau r\theta) + C_s$
a2y		$\frac{r}{\sin\gamma\cos\gamma} + 1 - 2n_y + B_c$	$+\frac{8\lambda_x n_y}{\theta r} + \frac{2\lambda_y r}{\theta n_y}$	$-\frac{\theta r}{4}\left(\frac{r}{2\sin\gamma\cos\gamma} + 1 - 2n_y\right) + C_c$	$-\lambda_x(1 + \frac{8n_y\mu\tau}{r\theta}) - \frac{\lambda_y r}{2n_y}(r + \frac{4\mu\tau}{\theta}) + C_s$
a2y'		$\frac{r}{\sin\gamma\cos\gamma} + 1 - 2n_y + B_c$	$+\frac{8\lambda_x n_y}{\theta r} + \frac{2\lambda_y r}{\theta n_y}$	$-\frac{\theta r}{4}\left(\frac{r}{2\sin\gamma\cos\gamma} + 1 - 2n_y\right) + C_c$	$-\lambda_x(2n_y + \frac{8n_y\mu\tau}{r\theta}) - \frac{\lambda_y r}{2n_y}(r + \frac{4\mu\tau}{\theta}) + C_s$
*a2y**		$\frac{r}{\sin\gamma\cos\gamma} + 1 - 2n_y + B_c$	$+\frac{8\lambda_x n_y}{\theta r}$	$-\frac{\theta r}{4}\left(\frac{r}{2\sin\gamma\cos\gamma} + 1 - 2n_y\right) + C_c$	$-\lambda_x(1 + \frac{8n_y\mu\tau}{r\theta}) - \frac{4\lambda_y\eta_y}{\theta^2} + C_s$
*a2y'**		$\frac{r}{\sin\gamma\cos\gamma} + 1 - 2n_y + B_c$	$+\frac{8\lambda_x n_y}{\theta r}$	$-\frac{\theta r}{4}\left(\frac{r}{2\sin\gamma\cos\gamma} + 1 - 2n_y\right) + C_c$	$-\lambda_x(2n_y + \frac{8n_y\mu\tau}{r\theta}) - \frac{4\lambda_y\eta_y}{\theta^2} + C_s$
*a2y***		$\frac{r}{\sin\gamma\cos\gamma} + 1 - 2n_y + B_c$	$+\frac{2\lambda_y r}{\theta n_y}$	$-\frac{\theta r}{4}\left(\frac{r}{2\sin\gamma\cos\gamma} + 1 - 2n_y\right) + C_c$	$-\frac{8\lambda_x\eta_x n_y}{r\theta^2} - \frac{\lambda_y r}{2n_y}(r + \frac{4\mu\tau}{\theta}) + C_s$
*a2y****		$\frac{r}{\sin\gamma\cos\gamma} + 1 - 2n_y + B_c$		$-\frac{\theta r}{4}\left(\frac{r}{2\sin\gamma\cos\gamma} + 1 - 2n_y\right) + C_c$	$-\frac{8\lambda_x\eta_x n_y}{r\theta^2} - \frac{4\lambda_y\eta_y}{\theta^2} + C_s$

The continuity terms are $B_c = k_{cx} + k_{cy}\frac{r^2}{2n_y}$, $C_c = -k_{cx}\tau - k_{cy}\frac{\tau r^2}{2n_y}$, $C_s = k_{cx}k_{rx}\lambda_x + k_{cy}k_{ry}\frac{r^2\lambda_y}{2n_y}$.

Table 7: y-aligned mechanisms: General form of each equation $a\psi_1^2 + b\psi_1 + c = 0$

Case	*a*	*b*	*c*
b1y	$\frac{1}{\theta \sin\gamma \cos\gamma}$	B_c	$-\frac{\lambda_x}{2} - \frac{\lambda_y r^2}{4n_y} + C_c + C_s$
b1y'	$\frac{1}{\theta \sin\gamma \cos\gamma}$	B_c	$-\lambda_x n_y - \frac{\lambda_y r^2}{4n_y} + C_c + C_s$
*b1y**	$\frac{1}{\theta \sin\gamma \cos\gamma}$	$-\frac{\lambda_y r}{\theta n_y} + B_c$	$-\frac{\lambda_x}{2} - \lambda_y(\frac{2\eta_y}{\theta^2} - \frac{\mu\tau r}{\theta n_y}) + C_c + C_s$
*b1y'**	$\frac{1}{\theta \sin\gamma \cos\gamma}$	$-\frac{\lambda_y r}{\theta n_y} + B_c$	$-\lambda_x n_y - \lambda_y(\frac{2\eta_y}{\theta^2} - \frac{\mu\tau r}{\theta n_y}) + C_c + C_s$
*b1y***	$\frac{1}{\theta \sin\gamma \cos\gamma}$	$-\frac{4\lambda_x n_y}{\theta r} + B_c$	$-\frac{4\lambda_x n_y}{\theta r}(\frac{\eta_x}{\theta} - \mu\tau) - \frac{\lambda_y r^2}{4n_y} + C_c + C_s$
*b1y****	$\frac{1}{\theta \sin\gamma \cos\gamma}$	$-\frac{4\lambda_x n_y}{\theta r} - \frac{\lambda_y r}{\theta n_y} + B_c$	$-\frac{4\lambda_x n_y}{\theta r}(\frac{\eta_x}{\theta} - \mu\tau) - \lambda_y(\frac{2\eta_y}{\theta^2} - \frac{\mu\tau r}{\theta n_y}) + C_c + C_s$
b2y	$\frac{1}{\theta \sin\gamma \cos\gamma}$	$\frac{4\lambda_x n_y}{\theta r} + \frac{\lambda_y r}{\theta n_y} + B_c$	$-\lambda_x(\frac{1}{2} + \frac{4\mu\tau n_y}{\theta r}) - \frac{\lambda_y r}{4n_y}(r + \frac{4\mu\tau}{\theta}) + C_c + C_s$
b2y'	$\frac{1}{\theta \sin\gamma \cos\gamma}$	$\frac{4\lambda_x n_y}{\theta r} + \frac{\lambda_y r}{\theta n_y} + B_c$	$-\lambda_x(n_y + \frac{4\mu\tau n_y}{\theta r}) - \frac{\lambda_y r}{4n_y}(r + \frac{4\mu\tau}{\theta}) + C_c + C_s$
*b2y**	$\frac{1}{\theta \sin\gamma \cos\gamma}$	$\frac{4\lambda_x n_y}{\theta r} + B_c$	$-\lambda_x(\frac{1}{2} + \frac{4\mu\tau n_y}{\theta r}) - \frac{2\lambda_y \eta_y}{\theta^2} + C_c + C_s$
*b2y'**	$\frac{1}{\theta \sin\gamma \cos\gamma}$	$\frac{4\lambda_x n_y}{\theta r} + B_c$	$-\lambda_x(n_y + \frac{4\mu\tau n_y}{\theta r}) - \frac{2\lambda_y \eta_y}{\theta^2} + C_c + C_s$
*b2y***	$\frac{1}{\theta \sin\gamma \cos\gamma}$	$\frac{\lambda_y r}{\theta n_y} + B_c$	$-\frac{4\lambda_x \eta_x n_y}{\theta^2 r} - \frac{\lambda_y r}{4n_y}(r + \frac{4\mu\tau}{\theta}) + C_c + C_s$
*b2y****	$\frac{1}{\theta \sin\gamma \cos\gamma}$	B_c	$-\frac{4\lambda_x \eta_x n_y}{\theta^2 r} - \frac{2\lambda_y \eta_y}{\theta^2} + C_c + C_s$

The continuity terms are $B_c = k_{cx} + k_{cy}\frac{r^2}{2n_y}$, $C_c = -k_{cx}\tau - k_{cy}\frac{\tau r^2}{2n_y}$, $C_s = k_{cx}k_{rx}\lambda_x + k_{cy}k_{ry}\frac{r^2\lambda_y}{2n_y}$.

Table 8: y-aligned mechanisms: General form of each equation $a\psi_1^2 + b\psi_1 + c = 0$

Case	*a*	*b*		*c*	
cy		$\frac{2\tau}{\theta \sin\gamma \cos\gamma} + B_c$	$+\frac{4\lambda_x n_y}{\theta r} + \frac{\lambda_y r}{\theta n_y}$	$-\frac{\tau^2}{\theta \sin\gamma \cos\gamma} + C_c$	$-\lambda_x(\frac{1}{2} + \frac{4\mu\tau n_y}{\theta r}) - \frac{\lambda_y r}{4n_y}(r + \frac{4\mu\tau}{\theta}) + C_s$
cy'		$\frac{2\tau}{\theta \sin\gamma \cos\gamma} + B_c$	$+\frac{4\lambda_x n_y}{\theta r} + \frac{\lambda_y r}{\theta n_y}$	$-\frac{\tau^2}{\theta \sin\gamma \cos\gamma} + C_c$	$-\lambda_x(n_y + \frac{4\mu\tau n_y}{\theta r}) - \frac{\lambda_y r}{4n_y}(r + \frac{4\mu\tau}{\theta}) + C_s$
*cy**		$\frac{2\tau}{\theta \sin\gamma \cos\gamma} + B_c$	$+\frac{4\lambda_x n_y}{\theta r}$	$-\frac{\tau^2}{\theta \sin\gamma \cos\gamma} + C_c$	$-\lambda_x(\frac{1}{2} + \frac{4\mu\tau n_y}{\theta r}) - \frac{2\lambda_y \eta_y}{\theta^2} + C_s$
cy'		$\frac{2\tau}{\theta \sin\gamma \cos\gamma} + B_c$	$+\frac{4\lambda_x n_y}{\theta r}$	$-\frac{\tau^2}{\theta \sin\gamma \cos\gamma} + C_c$	$-\lambda_x(n_y + \frac{4\mu\tau n_y}{\theta r}) - \frac{2\lambda_y \eta_y}{\theta^2} + C_s$
*cy***		$\frac{2\tau}{\theta \sin\gamma \cos\gamma} + B_c$	$+\frac{\lambda_y r}{\theta n_y}$	$-\frac{\tau^2}{\theta \sin\gamma \cos\gamma} + C_c$	$-\frac{4\lambda_x \eta_x n_y}{\theta^2 r} - \frac{\lambda_y r}{4n_y}(r + \frac{4\mu\tau}{\theta}) + C_s$
*cy****		$\frac{2\tau}{\theta \sin\gamma \cos\gamma} + B_c$		$-\frac{\tau^2}{\theta \sin\gamma \cos\gamma} + C_c$	$-\frac{4\lambda_x \eta_x n_y}{\theta^2 r} - \frac{2\lambda_y \eta_y}{\theta^2} + C_s$

The continuity terms are $B_c = k_{cx} + k_{cy}\frac{r^2}{2n_y}$, $C_c = -k_{cx}\tau - k_{cy}\frac{\tau r^2}{2n_y}$, $C_s = k_{cx}k_{rx}\lambda_x + k_{cy}k_{ry}\frac{r^2\lambda_y}{2n_y}$.

Table 9: Fracture crack-widths for meshes of ductility classes B and C used in case studies.

Mesh	Diameter (mm)	Type	Class	f_y (Mpa)	f_u (Mpa)	ε_u	l_d required (mm)	l_d' required (mm)	(l_d+l_d') required (mm)	No. of broken welds	Actual FCW (mm)
A142	6	Deformed	B	463	500	0.050	96.3	15.4	111.7	0	1.01
			C	435	500	0.075	90.4	27.1	117.6	0	2.27
	6	Smooth	B	463	500	0.100	321.0	51.4	372.4	0	5.43
			C	435	500	0.120	301.5	90.4	391.9	0	11.08
A193	7	Deformed	B	463	500	0.050	112.4	18.0	130.3	0	1.17
			C	435	500	0.075	105.5	31.7	137.2	0	2.63
	7	Smooth	B	463	500	0.100	374.5	59.9	434.4	0	6.27
			C	435	500	0.120	351.7	105.5	457.2	1	13.32
A252	8	Deformed	B	463	500	0.050	128.4	20.5	148.9	0	1.31
			C	435	500	0.075	120.6	36.2	156.8	0	2.98
	8	Smooth	B	463	500	0.100	428.0	68.5	496.5	0	7.13
			C	435	500	0.120	402.0	120.6	522.5	1	15.09
A393	10	Deformed	B	463	500	0.050	160.5	25.7	186.2	0	1.59
			C	435	500	0.075	150.7	45.2	196.0	0	3.67
	10	Smooth	B	463	500	0.100	535.0	85.6	620.6	0	8.80
			C	435	500	0.120	502.4	150.7	653.2	1	18.75
A566	12	Deformed	B	463	500	0.050	192.6	30.8	223.4	0	1.86
			C	435	500	0.075	180.9	54.3	235.1	0	4.35
	12	Smooth	B	463	500	0.100	642.0	102.7	744.7	1	10.89
			C	435	500	0.120	602.9	180.9	783.8	1	22.33